공학석사 학위논문

Flow effects on sea urchin fertilization

흐름이 성게 수정에 미치는 영향

2019 년 6 월

서울대학교 대학원

건설환경공학부

유 호 정

ABSTRACT

Complex hydrodynamic structures inside the benthic boundary layer influence various biological process of marine ethology. The external fertilization of sea urchins is one of the biological mechanism which highly depend on flow conditions of boundary layer. To explain fertilization process from perspective of mechanics, the analysis of fluid structure near sea urchins should be preceded. In general, turbulent boundary layers are developed near rough walls and behind streamline objects, and variations of flow structure generate complex hydrodynamic structures. Gametes released from sea urchins are transported via surrounding flow to reach collision and fertilization with different sex through complex interaction with hydrodynamic structures.

The main objective of corresponding study is to analyze the flow effects on sea urchin fertilization. Fertilization rate is explored for uni-directional flow with free stream velocity ranging from 0.025 to 0.2 m/s to analyze the effect of velocity on fertilization and relative contribution of different locations (aboral, wake, substrate, and water column). As velocity increases, fertilization decreases and wake had most influence on total fertilization in general. Corresponding study is progressed in three steps. First, hydrodynamic characteristics near sea urchin and trajectory of gametes are simulated through Lagrangian Particle Tracking. Second, actual eggs being fertilized are computed based on relative distance between gametes of different sex and nearby sperm concentration. Last, contribution of each location on fertilization is computed and fertilization process is explained by hydrodynamic structures around

sea urchin.

Corresponding study suggest mechanical perspective to understand biological process and Computational Fluid Dynamics (CFD) as possible tool to simulate fertilization process of sea urchins. The methods applied to this study can help analyze various engineering or scientific problems that are driven by turbulent mixing and reaction between particles. It suggests wider perspective and possibilities to study complex processes which requires analysis of both particles and background flow.

TABLE OF CONTENTS

List of Figures

List of Tables

List of Symbol

Latin Uppercase

C_D	Drag coefficient
C_s	WALE constant
D_m	Molecular diffusivity
D_p	Diameter of particle
$D_{i,E}$	Distance between individual egg to their averaged location
$D_{i,S}$	Distance between individual sperm to their averaged location
E_0	Initial egg concentration
F_B	Buoyancy force
F_C	Cohesion force
F_D	Drag force
F_G	Gravitational force
F_i	Blending function
F_P	Pressure force
I_d	Morista index
I_p	Standardized morista index
K	Turbulent diffusivity

L	Characteristic length
M_c	Clumped index
M_u	Uniform index
P_w	Rate of production of ω
Q	Constant rate of particle per second
Re_p	Reynolds number of particle diameter
Re_x	Reynolds number of distance from the origin in x-direction
Re_δ	Reynolds number of boundary layer thickness
S_o	Initial sperm concentration
S_e	Sperm concentration stuck to eggs
S_f	Free sperm concentration
$\overline{S}_{ij}$	Strain rate tensor of the resolved large eddy
ST	Strouhal number
St	Stokes number
T_i	Integral time scale
$\overline{T}(z)$	Temperature distribution
U	Free stream velocity

Latin Lowercase

ℓ	Concentration of particles

c_f	Skin friction
d_f	Particle diameter
e_{ij}	Fluctuation strain rate
$\overline{f}$	Additional body force
g	Gravitational acceleration
k	Turbulent kinetic energy
m_p	Mass of particles
n_s	Sample size
$\overline{p}$	Mean pressure
r	Radius
r_R	Ratio
$r(\tau)$	Autocorrelation function of time scale
$r(x)$	Autocorrelation function of length scale
t	Duration time
u_f	Velocity of fluid
u_p	Velocity of particle
$\overline{u}$	Mean velocity in x-direction
u^*	Shear velocity
u'	Velocity fluctuation component in x-direction
v'	Velocity fluctuation component in y-direction

x	Distance in x-direction
$x_{i,egg}{}^{t}$	Location of ith egg at time t
$\overline{x}_{egg}{}^{t}$	Location of ith egg at time t
$x_{i,sperm}{}^{t}$	Location of ith sperm at time t
$\overline{x}_{sperm}{}^{t}$	Location of ith sperm at time t
x	Distance in x-direction
y	Distance in y-direction
z	Distance in z-direction

Greek Uppercase

Φ	Total fertilization rate inside the domain for target duration time.

Greek Lowercase

α	Model constant
β	Fertilization cross-section of egg
β_0	Total cross-section of egg
δ	Thickness of boundary layer
ε	Turbulent energy dissipation
ε_e	Relative error measure

θ	Momentum thickness of boundary layer
κ	The Von Karman constant
κ^t	Kurtosis of distances among gametes
μ	Dynamic viscosity coefficient
$\mu_D{}^t$	Mean of distances among gametes
μ_t	Sub-grid scale turbulent viscosity
ν	Kinematic viscosity coefficient
ρ	Density
ρ_f	Density of fluid
ρ_p	Density of particle
σ	Variance
$\sigma_D{}^{2t}$	Variance of distances among gametes
τ	Shear stress
τ_e	Turnover time of large eddy
τ_F	Characteristic time of flow
τ_K	Kolmogorov time scale
τ_p	Particle response time
ω	Specific turbulent energy dissipation rate
ω_f	Frequency
$\chi_{0.025}{}^2$	Chi-squared value with (n-1) degree of freedom and 0.025 quantile

$\chi_{0.975}^{2}$ Chi-squared value with (n-1) degree of freedom and 0.975 quantile

CHAPTER 1. INTRODUCTION

1.1 General introduction

The survival of aquatic animals is highly dependent on hydrodynamics of surrounding water. Every mechanism of survival is directly related to flow conditions and marine species respond to surrounding fluid in either passive or active way (Fish 2006). Sea urchins which cling to sea floor and stay immotile for their lifetime, are passively influenced by surrounding flow conditions. Sea urchins have minimum organs for survival in harsh environments of benthic boundary layer, and due to their simple structures, the activity sea urchins execute during lifetime are quite limited.

Among few lifetime activities, reproduction is one of the major duty to maintain the survival of their species. Sea urchins fertilize by 'broadcast spawning' which is to release their gametes (i.e. sperms and eggs) into the water column and allow surrounding fluids to transport gametes for fertilization (James & Sikkavuopio). Since gametes soon loose motility after the release, magnitude of fertilization is determined by surrounding flow conditions. In uni-directional flows, gametes are transported by the current and turbulent diffusion inside the benthic boundary layer which bring eggs and sperms to collide and fertilize (Kregting et al., 2013). It is expected from precedent studies that optimal level of turbulent mixing exists for efficient collision and fertilization. If mixing is too rapid, gametes are excessively diluted and loss fertilizability. On the contrary, if turbulent mixing is too slow, contact

between sperms and eggs fails occur leading to less fertilization (Denny & Shibata 1989).

Due to the membrane generated at egg surface when fertilization occurs, whole process can be visualized and sea urchin fertilization rate can be quantified. Along with advantageous feature for efficient analysis, high dependence of sea urchin fertilization on surrounding flow led previous researches to analyze the complex interaction between fertilization and hydrodynamic structures. At initial stages of research, flow condition itself was considered as variable to determine the success of fertilization. Fertilization rate decreased as flow velocity increased (Thomas et al., 2013) and increased until optimal point and later decreased linearly as energy dissipation increased under constant shear stress (Mead & Denny 1995). Later researches concerned more on relative contribution of different locations (aboral, wake, substrate and water column) on fertilization. Although most fertilization occurred near the sea urchin surface, the relative contribution of each location varied by different flow conditions. (Kregting et al., 2014, Yund et al., not published).

In other areas of marine ethology, computational fluid dynamics method (CFD) is actively applied to analyze various mechanisms of marine life. 3D simulation of tadpole locomotion (Liu et al., 1997) and telemetry tag attached to dolphin (Pavlov et al., 2012) testify the capability of CFD as a tool to analyze behaviors of aquatic animals. Until now, research of sea urchin fertilization has been focused on laboratory experiments due to difficulties of simulating external fertilization through CFD. Possible difficulties include 1) simultaneous computation of gametes trajectories

along with background flow structures and 2) considering reaction mechanism between sperms and eggs at each time step. If such problems can be handled, introduction of CFD enables detailed analysis of sea urchin fertilization process. As locations for respective gametes become available at every time step, mixing gametes can be analyzed and their distribution can be quantified during whole fertilization process. Flow characteristics are provided for every position inside the simulation domain and thus, complex flow structures can be analyzed in detail. Interaction between fertilization and hydrodynamic structures are explored based on thorough understanding of gamete mixing and flow characteristics.

To handle numerical simulation including both continuous fluid and discrete particles (i.e. sperms and eggs), corresponding study selected Lagrangian Particle Tracking (LPT) algorithm which focus on providing the trajectory of each particles at every time-step (Fraga et al., 2016). Based on respective location of each gamete, distance between eggs and sperms are computed and by considering required sperm concentration to maintain fertilizability, the success of fertilization is identified. For different flow velocity, turbulent mixing of gametes and retention time vary due to the hydrodynamic conditions (Kregting et al., 2013) which derives varying fertilization rate and relative contribution of different locations.

Although corresponding study is focused on microscopic process in marine ethology, fertilization of sea urchins, the method applied to analyze particle mixing and fertilization can be further expanded to any engineering or scientific problems that are driven by turbulent mixing of particles and reaction. Successful introduction

3

of LPT algorithm and quantification of particle distribution suggests

1.2 Objectives

After gametes are released from sea urchins, they soon lose mobility and fully depend on surrounding fluid to be dispersed, contact with opposite sex, and become fertilized. It is evident that fertilization rate of sea urchins is correlated with surrounding hydrodynamic conditions and investigating such hydrodynamics is reasonable to understand fertilization mechanism of sea urchins. The objective of this study is to analyze the effect of flow on sea urchin fertilization based on detailed analysis of gamete trajectories and surrounding hydrodynamic structures for different flow velocity.

There are three specific goals to satisfy through corresponding study; 1) validate Lagrangian Particle Tracking algorithm as a reasonable tool to simulate mixing gametes. 2) quantify gamete distribution to understand fertilization rate 3) understand flow structures behind the sea urchin body to analyze relative contribution of different locations.

LPT algorithm incorporates advantages of Eulerian and Lagrangian perspectives to suggest reasonable tool to analyze particle-laden flows. LPT algorithm has been widely applied in engineering field and to broaden its application to wider research topics, the algorithm would be applied to simulate sea urchin fertilization process and its validity would be identified.

Since fertilization rely on collision between gametes of opposite sex and collision

is identified by respective position of gametes at each time step, distribution of gametes during simulation time should be explored to understand varying fertilization rate for different flow velocity. By analyzing the distance between gametes and computing the Morista index, the distribution of gametes would be quantified. Relationship between collision to gametes distribution and flow characteristics would be analyzed.

Benthic boundary layer is the region where morphological structures of sea floors affect the flow conditions which generates complex hydrodynamic structures and turbulent mixing of gametes. Majority of fertilization process occur inside boundary layer due to passive mobility of gametes requiring detailed analysis of flow in this region. By understanding the hydrodynamic structures behind sea urchin body inside the boundary layer, the flow characteristics of different locations can be computed and can be used to explain relative contribution of each location on fertilization.

Corresponding study rely on methods which can be generally applied to analysis of particle interaction inside flow. Thus, more general objective of this study would be to suggest a research paradigm to analyze various engineering or scientific problems related to mixing and reaction mechanism.

CHAPTER 2. THEORETICAL BACKGROUDS

2.1 Fertilization process of sea urchin

2.1.1 External fertilization of sea urchin

Sea urchins are primitive organisms lacking much of complex organs. They are only comprised of mouth, digestive organ, gonad (reproductive organ), and simple nervous system (James & Sikkavuopio, 2011). Their primitive structures are aimed for efficient survival in harsh environments of benthic boundary layer, focusing on systems directly related to survival of their species. Due to primitive reproduction systems, most appropriate reproduction mechanism would be external fertilization.

Most species of sea urchins have separate sexes and they release their gametes (eggs for females and sperms for males) in water column once in a year for reproduction, which is called broadcast spawning (James & Sikkavuopio, 2011). The size of eggs released by female sea urchins vary by the species and individuals, diameter ranging between $70-160\,\mu m$. Sperm size also vary between $6.0-7.0\,\mu m$ in length and $1.5-2.0\,\mu m$ in width (Levitan, 1993).

The success of external fertilization is heavily dependent on surrounding flow motion since sperms and eggs cannot encounter just by their own active movements (Denny & Shibata 1989). Compared of surround water conveying eggs and sperms, self-motility of gametes can be assumed as negligible. The habitat of sea urchins are usually highly turbulent areas where flow conditions vary in random manners.

2.1.2 Analytical models to explain external fertilization

The Vogel-Czihak-Chang-Wolf (VCCW) model is the most widely accepted fertilization kinetics model which predicts fertilization ratio for total volume based on initial egg concentration (E_0), sperm concentration (S_0) and duration time (t) (Vogel et al., 1982). This model is described by the following equation:

$$\Phi = 1 - \exp\left(\frac{\beta}{\beta_0} \frac{S_0}{E_0} \left(1 - \exp\left(-\beta_0 E_0 t\right)\right) \right) \tag{1}$$

where Φ is the fertilization ratio and β / β_0 is a constant to represent the fertilizable area of the egg. This model implies that fertilization ratio is dependent on the sperm and egg density which is later proved by laboratory experiments.

The mixing of gametes was analyzed in analogy to molecular diffusion to predict gamete concentration in respect to time and position. From the statistics of a two-dimensional random walk (Crank 1975), spatial distribution of concentration in thin layer can be represented as

$$c = \frac{Q}{4\pi D_m x} \exp\left(-\frac{(y^2 + z^2)\bar{u}}{4D_m x} \right) \tag{2}$$

Later turbulent diffusivity K replace the molecular diffusion coefficient D_m to reflect different magnitude between molecular diffusion and turbulent diffusivity and the concentration is estimated in the same manner as molecular diffusion.

$$c = \frac{Q}{4\pi K x} \exp\left(-\frac{(y^2 + z^2)\bar{u}}{4K x} \right) \tag{3}$$

However, the problem of the analogy is that molecular diffusion do not vary with

7

direction while turbulent diffusivity is determined by direction. To reflect such disparity, equation (2) can be rewritten as

$$c(x,y,z) = \frac{Q}{2\pi \bar{u} \sigma_y \sigma_z} \exp\left(-\frac{y^2}{2\sigma_y^2} + \frac{z^2}{2\sigma_z^2}\right) \tag{3}$$

where $\sigma_x = \alpha_x \frac{u_*}{\bar{u}} x^{\beta x}$, $\sigma_y = \alpha_y \frac{u_*}{\bar{u}} x^{\beta y}$, $\sigma_z = \alpha_z \frac{u_*}{\bar{u}} x^{\beta z}$ and α, β are calculated through experiments. Assuming that α_x, α_y and α_z are constant through time, $\beta_x = \beta_y = \beta_z = 1$, and $x = \bar{u}t$ we can derive equation (4)

$$\sigma_x \simeq \alpha_x \frac{u_*}{\bar{u}} x \simeq \alpha_x u_* t$$

$$\sigma_y \simeq \alpha_y \frac{u_*}{\bar{u}} y \simeq \alpha_y u_* t \tag{4}$$

$$\sigma_z \simeq \alpha_z \frac{u_*}{\bar{u}} z \simeq \alpha_z u_* t$$

Then concentration can be represented as function of distance from the point of release as equation (5) or function of time after release as equation (6)

$$c(x,y,z) = \frac{Q\bar{u}}{2\pi \alpha_y \alpha_z u_*^2 x^2} \exp\left(-\frac{y^2 \bar{u}^2}{2\alpha_y^2 u_*^2 x^2} + \frac{z^2 \bar{u}^2}{2\alpha_z^2 u_*^2 x^2}\right) \tag{5}$$

$$c(x,y,z) = \frac{Q}{2\pi \alpha_y \alpha_z u_*^2 t^2} \exp\left(-\frac{y^2}{2\alpha_y^2 u_*^2 t^2} + \frac{z^2}{2\alpha_z^2 u_*^2 t^2}\right) \tag{6}$$

2.1.3 Precedent and present research

External fertilization of sea urchins is a complicated process, influenced by a variety of physical, chemical and biological factors (Crimaldi 2012). Numerous precedent studies to analyze the dependence of fertilization success on such factors

are suggested in Tab.2.1.

Majorities of precedent research rely on laboratory experiments since visualization of fertilization process is available and number of fertilized eggs can be identified by existence of thin membrane generated at the surface of eggs. Diverse flow conditions have been analyzed through experiment including still water condition, uni-directional flow and oscillatory flow. Results from experiment suggest that complex interaction occurs between hydrodynamic structures and transported gametes to bring fertilization of sea urchins. Precedent studies that focus on total fertilization rate analyze the effect of mean velocity and turbulence properties. Later, researchers also analyzed the relative contribution of different locations on fertilization (aboral, wake, substrate, water column).

Numerical simulation to analyze sea urchin fertilization solves trajectories of particles that move in ideal vortex when flow properties are given by analytical solution. Current study aims to solve both flow and particle trajectories simultaneously since flows having analytical solutions are limited. In order to analyze sea urchin fertilization occurring at similar conditions to their actual habitat in nature, both flow fields and trajectories of gametes are required to be solved.

Table 2.1 Precedent and present studies

Reference	Topic	Method	Flow condition
Vogel et al. (1980)	Analytical model (VCCW model) to compute fertilization ratio based on gamete concentration	Analytical	-
Pennington (1985)	Estimation of sperm dilution and its effect on fertilization rate	Laboratory / Field experiment	Still water / unidirectional flow
Levitan et al. (1991)	Classification of sperm sea urchin distribution and its effect on fertilization rate	Laboratory experiment	Still water
Denny et al. (2002)	Effect of turbulence dissipation on fertilization rate	Laboratory experiment	Rotating flow
Crimaldi & Browing (2004)	Trajectories of gametes inside the vortex structure and its effect on fertilization	Numerical simulation	Ideal vortex
Thomas et al. (2013)	Flow structure inside unidirectional flow and its effect on fertilization rate	Laboratory experiment	Unidirectional flow
Kregting et al. (2013)	Flow structure inside oscillatory flow and its effect on fertilization rate	Laboratory experiment	Oscillatory flow
Kregting et al. (2014)	Comparison of fertilization rate between unidirectional and oscillatory flow	Laboratory experiment	Unidirectional/ Oscillatory flow
Present study (2019)	Analysis of flow structure and its effect on gamete concentration and fertilization rate	Numerical simulation	Unidirectional flow

2.2 Flow structure in the benthic boundary layer

2.2.1 Benthic boundary layer

Benthic boundary layers (BBL) are highly turbulent region which supply habitat for much of marine species. As mainstream flows over stationary sea floor, velocity gradient is established and forms the turbulent BBL, which magnitude range between 0.1 to 10 m. The thickness of BBL is proportional to the friction velocity and the oscillation period of mainstream velocity.

Numerous biological process occurs inside BBL including external fertilization between eggs and sperms of sea urchins. Fertilization of sea urchins occur close to seabed since sea urchins cling to sea floor and release gametes from their fixed bodies. Considering seabed as rough walls generating complex flow variations, boundary layer theory becomes applicable to analyze the flow characteristics near seabed.

Boundary layer thickness(δ) is defined as the height where velocity reaches free-stream velocity, $u/U = 1$. It can be represented as function of distance from the origin(x) by assuming one-seventh power law of Prandtl and Karman's momentum law as below equation (7):

$$\frac{\delta}{x} \approx \frac{0.16}{\text{Re}_x^{1/7}}$$

(7)

where Re_x is the Reynolds number based on distance from the origin.

When sea urchin bodies with spines are included into consideration, they increase the roughness of seabed and influence the flow passing by. The bluff bodies of sea urchin generate wake structures in the downstream due to the pressure gradient. Sea

11

urchin bodies changes not only the shape of boundary layer but also the overall hydrodynamic characteristics as well inside the boundary layer.

2.2.2 Flow structure behind a sea urchin

Inside the turbulent boundary layer behind sea urchin, flow characteristics vary by the position. Most conspicuous flow structure observed behind the bluff bodies in turbulent flows is vortex shedding, which is caused by excessive adverse pressure gradient (White 2008).

Assuming sea urchin body as having a shape of a hemisphere, pressure declines soon after flow pass by the sea urchin body and reaches the minimum point at the near top of the hemisphere. In such region where pressure gradient is large, separation occurs and vortex structures are generated (Savory & Toy 1986). A dimensionless parameter to measure the oscillating flow is the Strouhal number, which is defined as below:

$$ST = \frac{\omega L}{U} \tag{8}$$

where ω_f is the frequency, L is the characteristic length and U is the stream wise velocity.

In the near wake region behind sea urchin body, recirculation occurs generating a large backflow. It leads to decreased velocity magnitude at the very near wake region and as the distance from the origin of hemisphere increases, flow recovers its original properties. Since fluctuation of flow characteristics is the largest at the near wake region, the magnitude of turbulence, such as turbulence kinetic energy is also the largest at this region.

12

2.2.3 Turbulent motions

Complex flow structures behind the sea urchin intensifies the turbulence motions inside the benthic boundary layer. The nature of turbulent flows is that wide range of motions exist. Integral time scale and length scale is a representative scale among them which measures the memory of the turbulence. Integral time scale is estimated from autocorrelation function $r(\tau)$ of variable u_i as a function of time:

$$r(\tau) = \frac{\overline{u_i(t)u_i(t+\tau)}}{\overline{u_i}^2} \tag{9}$$

Fig.2 which is the typical autocorrelation plot suggests that $r(\tau)$ goes to 0 as $\tau \to \infty$ since the correlation with itself diminishes as time lag increases. The width of the correlation function can be computed by replacing the autocorrelation distribution with the rectangle of height 1, given as below equation (2):

$$T_i \equiv \int_0^\infty r(\tau)d\tau \tag{10}$$

Computed T_i is the integral time scale of the flow.
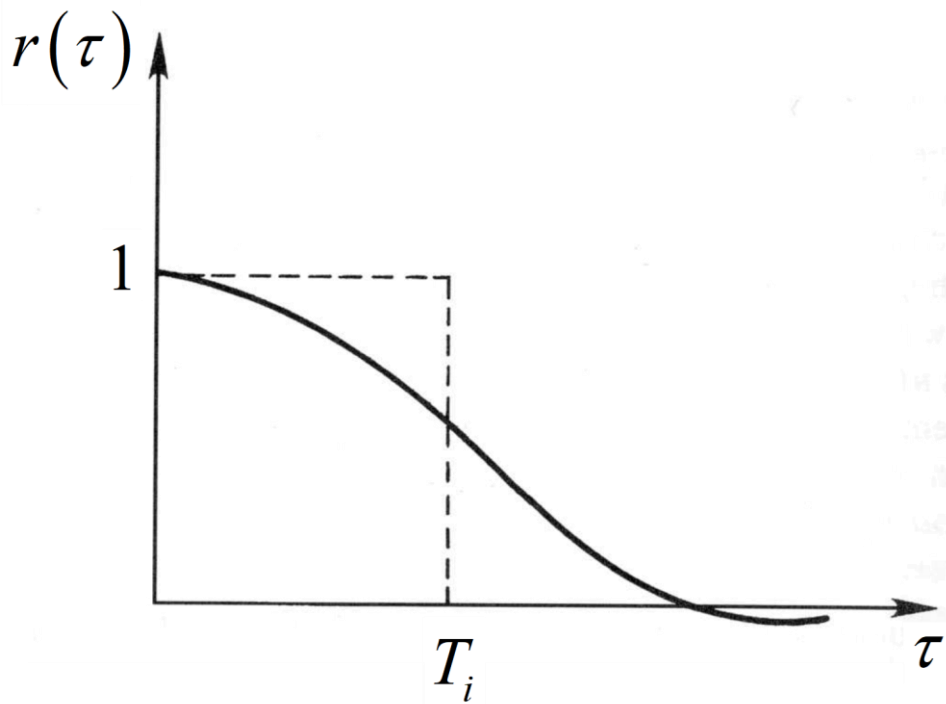
Figure 2.1 Autocorrleation function and the integral time scale.

Integral length scale can be computed in similar manner, but by defining autocorrelation function of variable u_i as function of space:

$$r(\mathbf{x}) = \frac{\overline{u_i(\mathbf{x}_0,t)u_i(\mathbf{x}_0+\mathbf{x},t)}}{\overline{u_i^2}} \tag{11}$$

Another method to compute integral length scale is to multiply integral time scale by point velocity based on G.I.Taylor's Frozen-In turbulence hypothesis (Taylor 1938). It states the advection of a field of turbulent past a fixed point can be taken as being mainly due to the larger, energy containing scales and suggests convenient linkage between the Eulerian and Lagrangian perspective of turbulence. Taylor's frozen turbulence approximation relates the spatial statistics to temporal statistics (Hill 1996).

In order to distinguish variables into mean part and deviation, Reynolds decomposition can be applied to each property:

$$u_i = U_i + u_i \tag{12}$$

where u_i is the instantaneous quantity, U_i is the mean field, and u_i is the fluctuation.

Turbulent kinetic energy (TKE) is computed based on fluctuation quantities as $\frac{1}{2}\overline{u_i^2}$, which represents the turbulent intensify of the flow. An equation for turbulent kinetic energy suggested below explains the life cycle of turbulence, from production to dissipation:

$$\frac{D}{Dt}\overline{\left(\frac{1}{2}u_i^2\right)} = -\frac{\partial}{\partial x_j}\left(\frac{1}{\rho_0}\overline{pu_j} + \frac{1}{2}\overline{u_i^2 u_j} - 2\nu\overline{u_i e_{ij}}\right) - \overline{u_i u_j}\frac{\partial U_i}{\partial x_j} + g\alpha\overline{wT'} - 2\nu\overline{e_{ij}e_{ij}} \qquad (13)$$

where $e_{ij} = \frac{1}{2}\left(\frac{\partial u_i}{\partial x_j} + \frac{\partial u_j}{\partial x_i}\right)$ is the fluctuation strain rate. Time derivative of turbulent

kinetic energy can be computed by the sum of spatial transport, shear production, buoyant production and viscous dissipation of turbulent kinetic energy.

First two terms on the right hand side are the spatial transport of turbulent kinetic energy by turbulence itself while third term represents the viscous transport. Fourth term is the rate of generation of turbulent kinetic energy generated by the interaction between Reynolds stress $(-\overline{u_i u_j})$ with the mean shear. Fifth term which is the buoyant production is determined based on the temperature distribution $\overline{T}(z)$. Last term is the viscous dissipation(ε) and has the order of the turbulence production terms in most locations.

2.3 Particle-laden flow

2.3.1 Introduction to particle-laden flow

Interaction between particle and background flow is determined based on Stokes number defined as $St = \frac{\tau_V}{\tau_p}$, where τ_p is the particle response time and τ_F is the characteristic time of the flow. Particle response time is defined as below equation (14):

$$\tau_p = \frac{\rho_p}{\rho} \frac{d_p^{\,2}}{18\nu} \tag{14}$$

where d_p is the particle diameter and ρ_p is the particle density. Characteristic time of the flow can be selected in either way; Kolmogorov time scale τ_K and or turnover time of large eddy τ_e

$$\tau_K = \left(\frac{\nu}{\varepsilon}\right)^{0.5} \tag{15}$$

$$\tau_e = \frac{l}{u} \tag{16}$$

When $St \ll 1$, particles and fluid are in near equilibrium and particle motions depend on flow characteristics. On the other hand, when $St \gg 1$, particles are unaffected by the fluid motion and particle inertia becomes important factor of particle movements.

The volume fraction of particles, $\Phi_p = \frac{MV_p}{V}$ determine the interaction between particles and turbulence of flow. For low volume fraction, $\Phi_p \leq 10^{-6}$, particle dispersion rely on turbulence while have the momentum transfer from particles to flow is negligible due to low concentration of particles. The interaction is termed as 'one way coupling'. In the second regime of volume fraction, $10^{-6} < \Phi_p \leq 10^{-3}$, momentum transfer from particles to turbulence is large enough to alter turbulence structure and the interaction is called as 'two way coupling'. When volume fraction further increases and reaches $10^{-3} < \Phi_p$, 'four way coupling' interaction occurs

17

which implies that frequent collision between particles affect both particle dispersion and turbulence. Fig. 2.2 show overall interaction between particles and flow.
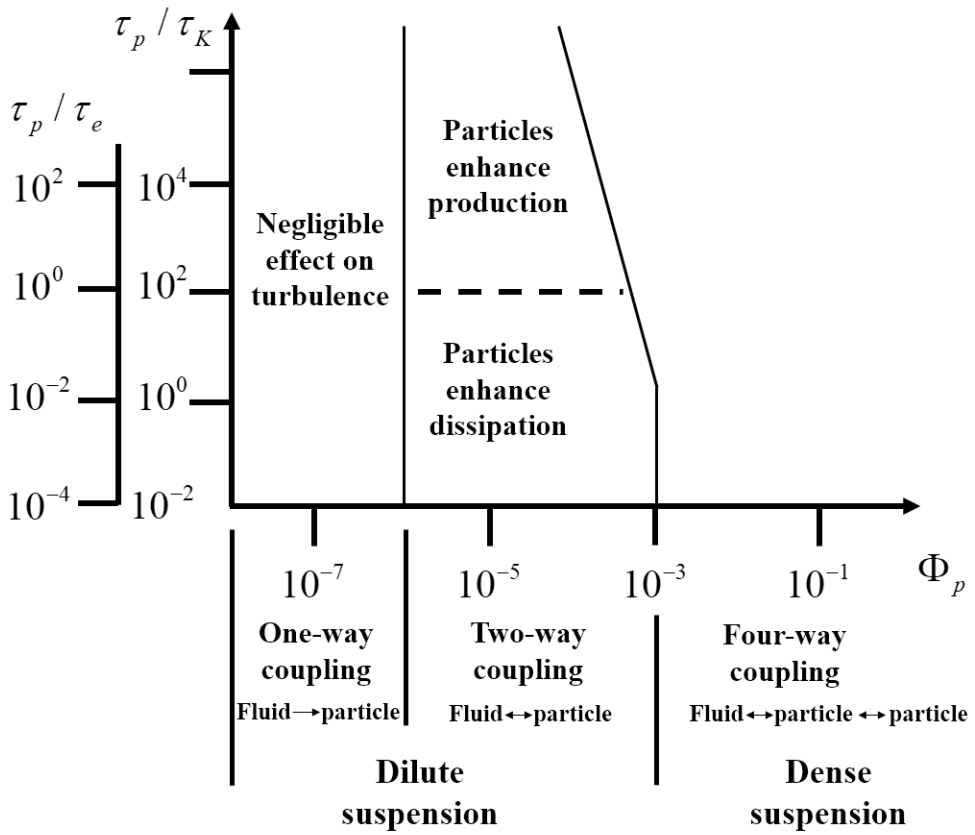
Figure 2.2 Map to identify the interaction between particles and turbulence.

2.3.2 Quantification of particle distribution

In order to quantify the distribution of gametes, the distance between individual gamete to averaged location of eggs and sperms is computed as below at each time step:

$$D_{i,S}{}^t = \mathbf{x}_{i,sperm}{}^t - \overline{\mathbf{x}}_{sperm}{}^t \tag{17}$$

$$D_{i,E}{}^t = \mathbf{x}_{i,egg}{}^t - \overline{\mathbf{x}}_{egg}{}^t \tag{18}$$

where $D_{i,S}{}^t$ is the distance between the location of ith sperm ($x_{i,sperm}$) and the mean location of every sperm ($\overline{\mathbf{x}}_{sperm}$) and $D_{i,E}{}^t$ is the distance between the location of ith egg ($x_{i,egg}$) and the mean location of every egg ($\overline{\mathbf{x}}_{egg}$) at time step t.

Statistical values for $D_{i,S}{}^t$ and $D_{i,E}{}^t$ (mean, variance and kurtosis) represent the distribution of distances among gametes which also shows the distribution of particles.

$$\mu_D{}^t = \sum_{i=1}^{n} \frac{D_i{}^t}{n} \tag{19}$$

$$\sigma_D{}^{2t} = \frac{\sum_{i=1}^{n} \left(D_i{}^t - \mu_D{}^t \right)^2}{n} \tag{20}$$

$$\kappa^t = \frac{\dfrac{\sum_{i=1}^{n} \left(D_i{}^t - \mu_D{}^t \right)^4}{n}}{\left(\dfrac{\sum_{i=1}^{n} \left(D_i{}^t - \mu_D{}^t \right)^2}{n} \right)^2} \tag{21}$$

Variance is the most common measure of the dispersion. If variance is large, it represents that wide range of distance between particles exist and thus, particles are

distributed for wide area. Kurtosis is the measure of peakedness and refers to the extent of peakedness or flatness of a distribution in comparison with the normal probability distribution. If the coefficient of kurtosis is greater than three, the distribution is more concentrated than normal distribution and vice versa. When kurtosis is large, distance between particles are concentrated to certain value. It means that particles are clumped at specific locations and their distributions inside the simulation domain show heterogeneous pattern rather than being uniformly distributed. Kurtosis roughly estimates the heterogeneity of particle distributions.

Another method to represent particle distribution is to introduce standardized Morisita index, which quantifies the spatial pattern to identify the inhomogeneity of distributions (Smith-Gill 1975). This index is widely used in ecological studies. The first step is to calculate Morisita's index as follows:

$$I_d = n_s \left[\frac{\sum x^2 - \sum x}{\left(\sum x \right)^2 - \sum x} \right]$$

(22)

where, I_d is Morisita's index, n_s is sample size, $\sum x$ is the sum of counts in each sample and $\sum x^2$ is the sum of counts squared in each sample. The second step is to estimate the uniform (M_u) and clumped (M_c) indices from following formulas:

$$M_u = \frac{\chi_{0.975}^2 - n_s + \sum x}{\left(\sum x \right) - 1}$$

(23)

$$M_c = \frac{\chi_{0.025}^2 - n_s + \sum x}{\left(\sum x\right) - 1} \qquad (24)$$

where, $\chi_{0.975}^2$ and $\chi_{0.025}^2$ are the chi-squared values with ($n_s - 1$) degree of freedom that have quantile values of 0.975 and 0.025, respectively. The third step is to calculate the standardized Morisita index, I_p, by comparing the magnitude of the uniform and clumped indices with the Morisita index as follows:

$$\text{When, } I_d \geq M_c > 1.0 \ : \ I_p = \left(\frac{I_d - M_c}{n_s - M_c}\right) \qquad (25)$$

$$\text{When, } 1.0 > M_u > I_d \ : \ I_p = \left(\frac{I_d - M_u}{M_u}\right) \qquad (26)$$

The spatial pattern can be evaluated from I_p which has a range from -1 to 1. As I_p approaches 1, particle are clumped in groups and their distributions show heterogeneous patterns. As I_p decreases, particles are distributed homogenously in the simulation domain and show random or uniform distribution.

CHAPTER 3. METHODOLOGY

3.1 Numerical model description

Complex fluid flows with no analytical solutions are handled in either way; experiment or numerical simulation. Among two approaches, numerical simulation has advantage that fluid flow of any condition can be analyzed and simulation technique can be varied by the objective of research. Fertilization process of sea urchin is a complex mechanism which results from mixing of gametes and interaction between opposite sex. Since whole process depend on surrounding hydrodynamics, both characteristics of particle and fluid need to be investigated go understand and analyze fertilization mechanism of sea urchin.

In general, two methods exist to solve particle transport in CFD simulations; Eulerian approach and Lagrangian approach. The selection between two approaches strictly depend on the objective of research. The ultimate goal of this study is to obtain trajectories of gametes and analyze the relationship between fertilization and flow characteristics. In such cases, when specific position of each particle are crucial results of simulation, Lagrangian approach becomes a better option to choose (Zang & Chen 2006). Precedent numerical studies that relied on turbulent eddy viscosity model predicted fertilization rates of only 0.01 – 1 % due to strong time-averaging turbulent dilution of gametes, and thus LPT algorithm is more suitable.

Among various turbulence models, Large Eddy Simulation (LES) model is

selected for corresponding study to satisfy both efficiency of simulation and accuracy of turbulence properties.

3.1.1 Governing equations for fluid motion

The basic governing equations of OpenFOAM to solve continuous fluid phase are mass and momentum conservation equations as follows:

$$\frac{\partial \rho}{\partial t} + \frac{\partial (\rho u_j)}{\partial x_j} = 0 \tag{27}$$

$$\frac{\partial (\rho u_i)}{\partial t} + \frac{\partial (\rho u_i u_j)}{\partial x_j} = -\frac{\partial p}{\partial x_i} + \frac{\partial}{\partial x_j}\left(\mu \frac{\partial u_i}{\partial x_j}\right) \tag{28}$$

Applying spatial filtering approach to separate the resolved (large-eddy) field from the small-eddy (sub-grid) field (Argyropoulos & Markatos 2014) gives LES equations as follows:

$$\frac{\partial \rho}{\partial t} + \frac{\partial (\rho \overline{u}_j)}{\partial x_j} = 0 \tag{29}$$

$$\frac{\partial (\rho \overline{u}_i)}{\partial t} + \frac{\partial (\rho \overline{u}_i \overline{u}_j)}{\partial x_j} = -\frac{\partial \overline{p}}{\partial x_i} + \frac{\partial}{\partial x_j}\left(\mu \frac{\partial \overline{u}_i}{\partial x_j}\right) - \frac{\partial \tau_{ij}}{\partial x} \tag{31}$$

where the over-bars are filtered quantities. Compared to Eqn. 28, Eqn. 31 has an extra non-linear term

$$\tau_{ij} = \rho \left(\overline{u_i u_j} - \overline{u}_i \overline{u}_j\right) \tag{32}$$

which is the Sub-Grid Scale (SGS) stress required to be modeled. Commonly, eddy-viscosity model is applied to solve the SGS stress, which assumes that SGS stress is proportional to the strain rate tensor of the filtered flow, $\overline{S}_{ij}$.

$$\tau_{ij} - \frac{1}{3}\tau_{kk}\delta_{ij} = -2\mu_t \overline{S}_{ij} \tag{33}$$

where $\overline{S}_{ij}$ is the strain rate tensor for the resolved large-eddy scale and μ_t is the sub-grid scale turbulent viscosity. Both $\overline{S}_{ij}$ and μ_t needs to be computed and for corresponding study, wall-adapting local eddy-viscosity (WALE) model is selected for closure model. WALE model recovers appropriate wall-asymptotic near-wall scaling for eddy viscosity without requiring dynamic procedure (Nicoud & Ducros 1999). SCS turbulent viscosity and strain rate tensor for resolved scales are modeled as follows (Ji et al. 2013):

$$\mu_t = \rho L_s^{\,2} \frac{\left(S_{ij}^{\,d} S_{ij}^{\,d}\right)^{3/2}}{\left(\overline{S}_{ij}\overline{S}_{ij}\right)^{5/2} + \left(S_{ij}^{\,d} S_{ij}^{\,d}\right)^{5/4}} \tag{34}$$

$$\overline{S}_{ij} = \frac{1}{2}\left(\frac{\partial \overline{u}_i}{\partial x_j} + \frac{\partial \overline{u}_j}{\partial x_i}\right) \tag{35}$$

$$S_{ij}^{\,d} = \frac{1}{2}\left(\overline{g}_{ij}^{\,2} + \overline{g}_{ji}^{\,2}\right) - \frac{1}{3}\delta_{ij}\overline{g}_{kk}^{\,2}, \quad \overline{g}_{ij} = \frac{\partial \overline{u}_i}{\partial x_j}, \quad L_s = \min\left(kd, C_s V^{1/3}\right) \tag{36}$$

where L_s is the mixing length applied for SGS, d is the distance from the closest wall, V is the computational grid volume and C_s is the WALE constant.

3.1.2 Lagrangian particle tracking

The motility of gametes is considered negligible since background flow velocity reaches and gametes are considered as passive scalars (Crimaldi & Zimmer 2014). The order of coupling between continuous phase (fluid motion) and discrete phase (particle motion) are determined by the volume fraction of discrete phase inside the

control volume (Eloghobashi 1994). The number of injected eggs and sperms are 10^4 and 10^5 respectively and considering the dimension of eggs and sperms suggested in chapter 2, the volume ratio of each gametes are computed as below:

Egg volume fraction: $\dfrac{10^4 \times \dfrac{4}{3}\pi(150\,\mu m)^3}{2\times 0.15\times 0.2} = 2.36\times 10^{-6}$ (37)

Sperm volume fraction: $\dfrac{10^5 \times \dfrac{4}{3}\pi(1\,\mu m)^3}{2\times 0.15\times 0.2} = 2.22\times 10^{-12}$ (38)

Although egg volume fraction is larger than 10^{-6}, we assume one way coupling interaction between particle and turbulence to compute trajectories of both egg and sperm for simplicity of numerical simulation.

In CFD modeling, particles are treated as point masses, and governing equation s for particles are as below.

$$\frac{d\underline{x}_p}{dt} = \underline{u}_p \tag{39}$$

$$m_p \cdot \frac{d\underline{x}_p}{dt} = \sum \underline{F}_i \tag{40}$$

In the momentum equation, $\sum \underline{F}_i$ represents the sum of all relevant forces and for corresponding study, drag force, buoyancy force, gravitational forces and pressure gradient force are included.

$$\sum \underline{F}_i = \underline{F}_D + \underline{F}_B + \underline{F}_G + \underline{F}_P \tag{41}$$

The drag force of particle are computed by following Eqn. 42 where drag coefficient, C_D is computed as Eqn. 42 as follows:

26

$$\underline{F}_D = C_D \frac{\pi D_p^2}{8} \rho_f \left(\underline{u}_f - \underline{u}_p \right) \left| \underline{u}_f - \underline{u}_p \right| \tag{42}$$

$$C_D = \begin{cases} \dfrac{24}{\mathrm{Re}_p} \left(1 + 0.15 \mathrm{Re}_p^{0.687} \right) & \mathrm{Re}_p \leq 1000 \\ 0.44 & \mathrm{Re}_p \leq 1000 \end{cases} \tag{43}$$

Gravity and buoyancy force is computed as one total force as Eqn. 44

$$\underline{F}_B + \underline{F}_G = m_p \underline{g} \left(1 - \frac{\rho_f}{\rho_p} \right) \tag{44}$$

Force due to pressure gradient is computed as Eqn. 45. If we substitute the pressure gradient from momentum equation of fluid to ∇p, Eqn. 45 is revised as Eqn. 46 (Greifzu et al. 2016).

$$\underline{F}_p = -\frac{\pi D_p^3}{6} \nabla p \tag{45}$$

$$\underline{F}_p = -\frac{\pi D_p^3}{6} \left(\frac{d\underline{u}_f}{dt} - \nabla \cdot \nu \left(\nabla \underline{u}_f + \nabla \underline{u}_f^T \right) \right) \tag{46}$$

3.1.3 Contact and fertilization detection algorithm.

It is defined that contact between sperms and eggs have occurred when sperms locate inside the jelly coat of eggs. By computing the relative distance between sperm and egg based on the position of each gamete, contact occurs when

$$\left| \mathbf{x}_{egg}{}^i(t) - \mathbf{x}_{sperm}{}^j(t) \right| \leq r_{egg} + r_{sperm} + r_{jellycoat} \tag{47}$$

where $\mathbf{x}_{egg}{}^i(t)$ and $\mathbf{x}_{sperm}{}^j(t)$ are the position of ith egg and j^{th} sperm at time t. r_{egg}, r_{sperm} and $r_{jellycoat}$ each specifies the radius of egg, sperm and egg jelly coat.

Assuming jelly coat diameter as equal to the egg diameter (Farley and Levitan 2001; Inamdar et al., 2007), target diameter to decide contact between egg and sperm becomes $602\,\mu m$.

$$d_c = 2 \times (r_{egg} + r_{sperm} + r_{jelly\,coat}) = 602\,\mu m \tag{48}$$

To ensure that possible contact between eggs and sperms are counted, time step varies for background flow velocity which is computed as below Eqn. 49 and time step corresponding to each inlet velocity is suggested by Tab.2

$$\Delta t \le \frac{d_t}{V} \tag{49}$$

Table 3.1 Time step for each inlet flow velocity

Velocity (m /s)	0.025	0.05	0.1	0.125	0.16	0.2
Time step (s)	0.02	0.01	0.005	0.004	0.0032	0.0025

For fertilization to occur, additional condition must be satisfied; sperm number density per unit volume should exceed $10^6 / l$ (Penington 1985). When sperm density is lower than $10^6 / l$, fertilizabiltiy of sperms is lost and contact between gametes does not further develop into fertilization process. To calculate sperm density, target radius around the contact pair of sperm and egg is selected and number of sperms inside the target radius is counted. Target radius is selected as equal to the radius of egg. Number of sperms inside the target volume is counted as below:

$$\left| \mathbf{x}_{sperm}{}^{i}(t) - \mathbf{x}_{contact}{}^{j}(t) \right| \leq 2r_{egg} \tag{50}$$

when sperm density inside the target volume should satisfy below condition:

$$\frac{N_{sperm}}{\frac{4}{3}\pi(2r_{egg})^3} \geq 10^6 \ sperms / l \tag{51}$$

Sperm and egg are removed from the control volume immediately when they fertilize with opposite sex so that overlapping of fertilization is prevented. In such scheme, total number of gametes decreases as simulation time and number of fertilized gametes increases.

3.2 Simulation setup

Schematic diagram depicts the geometry and boundary conditions applied to numerical simulation of sea urchin fertilization (Fig.3.1). Fluid velocity vary from range of 0.025 ~ 0.2 m/s, entering from fluid inlet with fixed velocity as a Dirichlet boundary condition and leaving at the fluid outlet by Neumann boundary condition. Bottom and side walls have no –slip wall condition. For simplicity of numerical simulation, sea urchins are assumed to have shape of hemisphere without spines but having no-slip boundary condition. In real nature, gametes are trapped near sea urchin body due to the spines and no-slip boundary condition is expected to result similar effect on the gamete trajectories.

Male sea urchin is located 0.5 m away from the inlet, so that flow structures are stabilized in the upstream of sea urchin body. Female sea urchin is positioned 0.5 m away from male urchin for well mixed sperms to encounter eggs. The length of the test section where actual contact and fertilization between eggs and sperms occur, which is the downstream of the female sea urchin body, is 1 m.

Sperm are injected at the time step when flow stow structures become stationary. Assuming sperm injection time as the initial time, egg injection time is determined by the time when the leading group of sperms first reach where female sea urchin is located (Tab3.2). Both sperm and egg have initial injection velocity in vertical direction as 0.05 m/s. Total simulation time was determined by the number of sperms left inside the simulation domain. When number of left sperms were lower than 5% of total injected sperms, simulation ended.
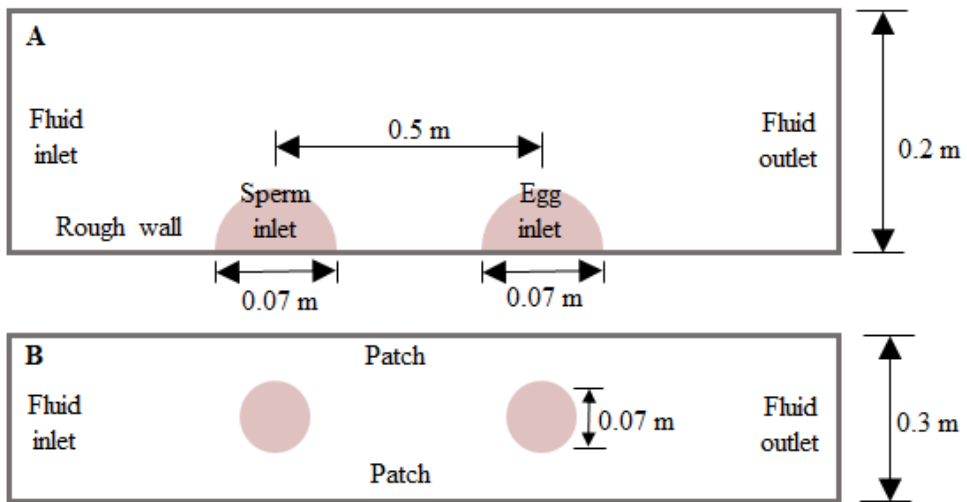
Figure 3.1 Simulation domain and boundary conditions (A) domain from top view.

(B) domain from front view

Table 3.2 Egg injection time

Velocity (m /s)	0.025	0.05	0.1	0.125	0.16	0.2
injection time (s)	20	10	5	4	3.12	2.5

3.3 Model validation

3.3.1 Model convergence

Particles locate downstream of the male sea urchin body and the interaction between gametes occur at the downstream of female sea urchin body. To focus on the contact between gametes and fertilization process, downstream regions have fine grid size while upstream have comparatively coarse grid size (Fig 3.2).

Since one-way coupling interaction is assumed for turbulence and gametes, grid convergence of the velocity field solution guarantees convergence for both particle trajectories and flow characteristics (Longest & Vinchurkar 2007). By considering the successive refinements on identical domain, the relative error measure of velocity magnitude between the coarse and fine solutions can be computed as below:

$$\varepsilon_e = \left| \frac{u_{i,coarse} - u_{i,fine}}{u_{i,fine}} \right|$$

(52)

where ε is the relative error measure, $u_{i,coarse}$ is the velocity at i^{th} grid computed from coarse grid and $u_{i,fine}$ from fine grid. Relative error value is determined for 1000 consistent points inside the simulation domain and root-mean-square error is computed as below:

$$\varepsilon_{rms} = \left(\frac{\sum_{i=1}^{10^3} \varepsilon_i^2}{10^3} \right)^{1/2}$$

(53)

The relative error value is invalid when grid refinement factor, r, is less than two due to the dependence on order of discretization method as well as grid refinement factor.

The grid convergence index (GCI) based on Richardson extrapolation suggest possibility to compute grid convergence even when r is less than two by equation suggested below (Roache 1994):

$$GCI[fine] = F_s \frac{\varepsilon_{rms}}{r^p - 1} \qquad (54)$$

where F_s is the safety factor and p is the order of discretization method. In corresponding study, $p = 2$ and F_s is selected as 3. Since grid refinement varies by each direction, it is computed as below by the ratio of control volumes in the fine and coarse meshes:

$$r_R = \left(\frac{N_{fine}}{N_{coarse}} \right)^{1/3} \qquad (55)$$

Tab 3.3 shows that grid convergence is obtained when grid size is smaller than 0.03 m since GCI values are lower than 5 % for every successive grid size refinement cases. For efficiency, the largest grid size 3 cm is selected for upstream region where no particles are injected. The region located between female sea urchin and male sea urchin have
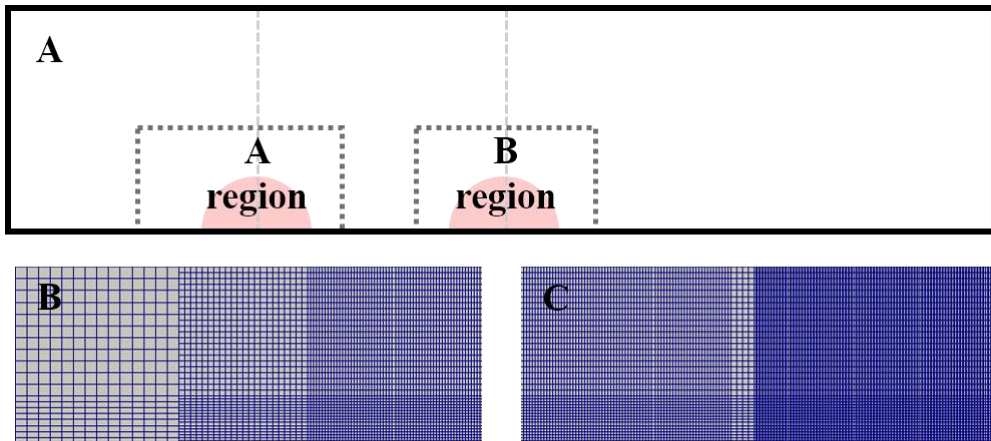
Figure 3.2 Grid size of simulation domain (A) Simulation domain (B) Grid size of
A region; grid size changes from 1 cm to 0.5cm at the location of male sea urchin
body. (C) Grid size of B region; grid size changes from 0.5 cm to 0.25 cm at the
location of male sea urchin body.

Table 3.3 Grid convergence

Grid size ($\times 10^3$)	r	ε_{rms} (%)	GCI (%)
30 – 12	1.55	0.999	2.142
12 – 2	1.5	1.001	2.421
2 – 1.2	1.41	1.004	3.013

3.3.3 Comparison with laboratory experiment

The experiment was conducted in the hydraulic laboratory of Seoul National University. A flume tank has size of 8 m long, 0.6 m wide, and 0.5 m depth with a pump deriving the flow. An objects with hemisphere shape resembling sea urchin with 0.08 m of diameter was located in the middle of the flume. The depth of flow was adjusted by installing a vertical wall perpendicular to the flow direction downstream from where the sea urchin was, to generate identical velocity with the simulation condition (Fig 3.3A).

Since particle trajectories do not influence fluid flow in one-way coupling simulation, flow structures behind the hemisphere in the absence of particles were analyzed to compare and validate the results of simulation. Velocity are measured with Acoustic Doppler Velocimetry (Nortek 2009) (Fig 3.3B).
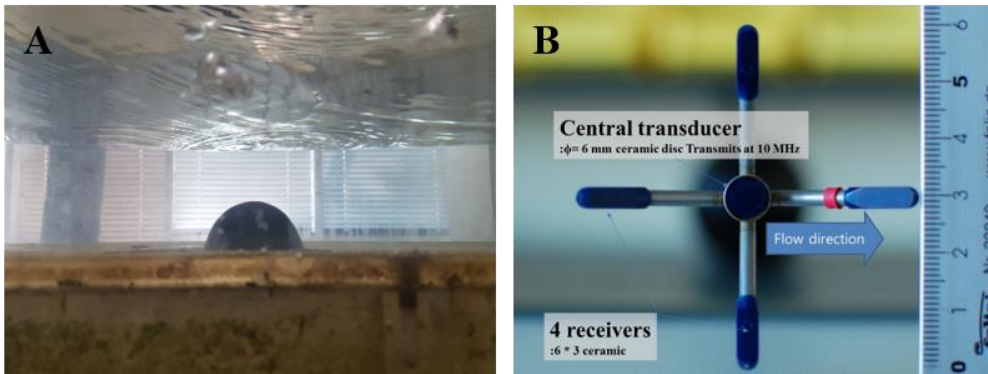
Figure 3.3 Experiment setup. (A) Front view of experiment geometry (B) Acoustic

Doppler Velocimetry (Nortek)

Vertical velocity profile for two stream-wise position for both experiment and simulation are provided as a validation data (Fig 3.4). r^2 between simulation and experiment for both two cases exceed 0.9, which show that simulation well reflects actual flow behind hemisphere. Backflow is generated at the behind of sea urchin body and recovers original inlet velocity near the free surface. The magnitude of backflow decreases as distance from the sea urchin body increases.

Velocity contours for y-z plane obtained from experiment and simulation are suggested below (Fig 3.5). Backflow is generated behind the hemisphere and vortex shedding structures appear behind the sea urchin body for both methods. Although larger fluctuations are observed from the experiment data compared to the simulation data, general structure including the wake length and velocity magnitude of simulation domain between two methods corresponds. It can be confirmed that the effect of sea urchin body on flow are well computed from numerical simulation by comparing with experiment data.
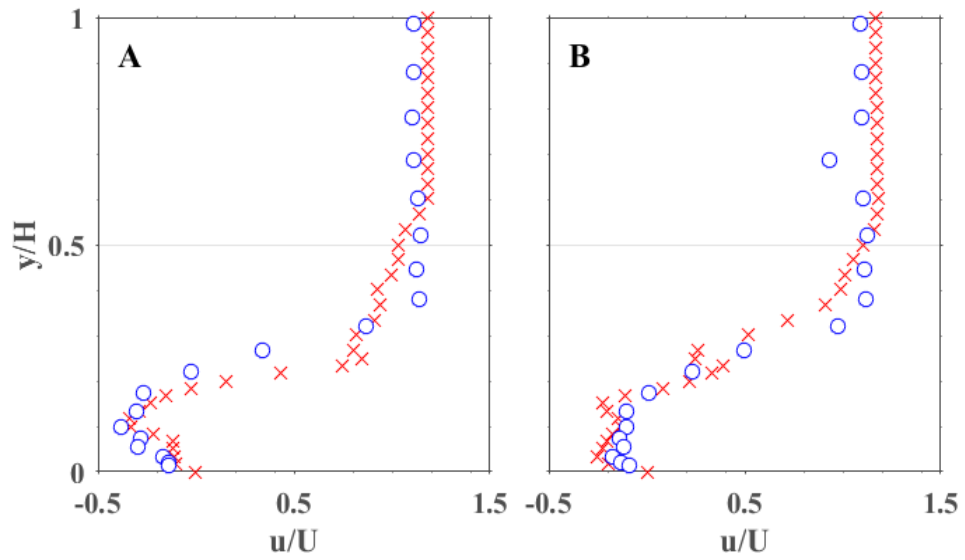
Figure 3.4 Validation result of non-dimensional vertical velocity profile, ○:
experiment result, ✖ : simulation result. (A) 0.07 m downstream from origin of
hemisphere. ($r^2 = 0.96$). (B) 0.1 m downstream from origin of hemisphere ($r^2 =$
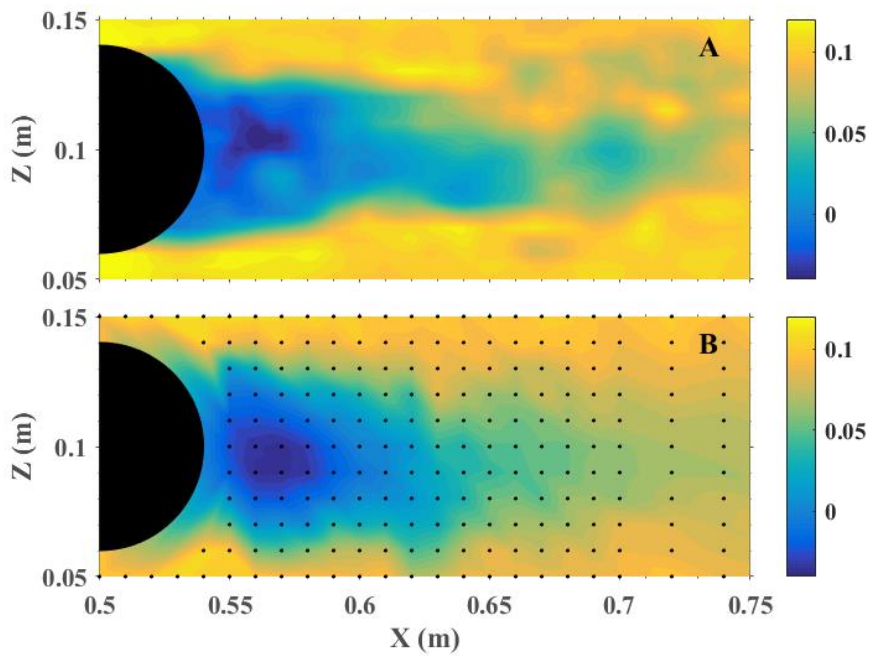0.98).

Figure 3.5 Instant velocity contour of y-z plane for y = 0.02 m. (A) Experiment

data. (B) Simulation data; black dots represent the positions where velocity is

measured and linear interpolation is applied to obtain contours

CHAPTER 4. RESULTS AND DISCUSSION

4.1 Collision and fertilization

The mixing of gametes due to surrounding flow structures lead to collision between eggs and gametes. When sperm number density per unit volume exceed $10^6 / l$, fertilization occurs. Fig 4.1 suggest collision rate and fertilization rate corresponding to varying flow velocity.

For every case, 10,000 eggs are injected from the female sea urchin body. Contact rate and fertilization rate are defined as

$$Contact\ rate\ (\%) = \frac{Eggs\ that\ collided\ with\ sperms}{Total\ eggs} \times 100 \qquad (56)$$

$$Fertilization\ rate\ (\%) = \frac{Eggs\ that\ fertilized\ with\ sperms}{Total\ eggs} \times 100 \qquad (57)$$
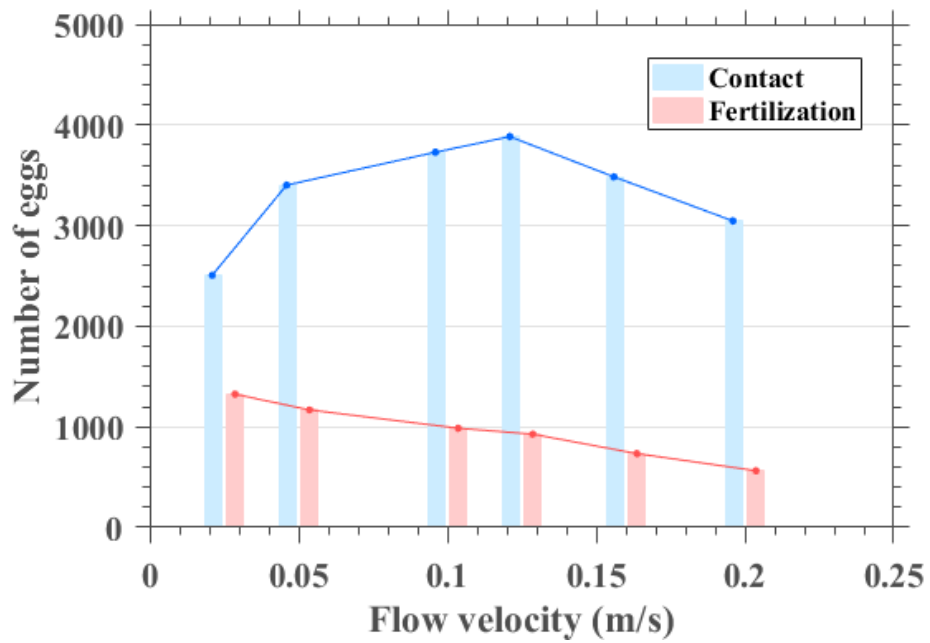
and the rates are suggested in Tab 4.1.

Figure 4.1 Number of eggs that collided or fertilized with sperms.

Table 4.1 Contact and fertilization rate

Flow velocity (m/s)	0.025	0.05	0.1	0.125	0.16	0.2
Contact rate (%)	25.06	34.02	37.29	38.84	34.84	30.46
Fertilization rate (%)	13.24	11.68	9.86	9.27	7.34	5.64

Contact rate ranges between 25% to 39% while fertilization rate range between 6% to 14%. Contact rate increases until flow velocity reaches 0.125 m/s and starts to decrease for faster flow velocity while fertilization rate steadily decreases with increasing flow speed. It implies that although both contact and fertilization occurs when gametes of different sexes collide together, different flow characteristic act as a driving force for each mechanism. Inverse relationship between fertilization rate and flow velocity has been discussed by precedent studies (Thomas et al., 2012) and corresponding study aims to explain the procedures of fertilization based on surrounding flow characteristics.

Fig 4.2 and Fig 4.3 shows the position where fertilization occurs during the entire simulation period. The location having darker dots represent the area of high fertilization. For lowest flow velocity, 0.25 m/s, most of the fertilization process occurs near the sea urchin body and fertilization location are concentrated in the centerline of the domain. As the flow velocity increases gradually, the length of dark-colored spot becomes shorter and fertilization locations are spread through the whole width of the domain at the downstream (Fig 4.2). Buoyant gametes are less likely to be fertilized at fast velocity. Except for the lowest velocity case, fertilization rarely occurs inside the recirculation region and the most fertilization happens at the height of 0.04 ~ 0.05 m from the bottom (Fig 4.3).
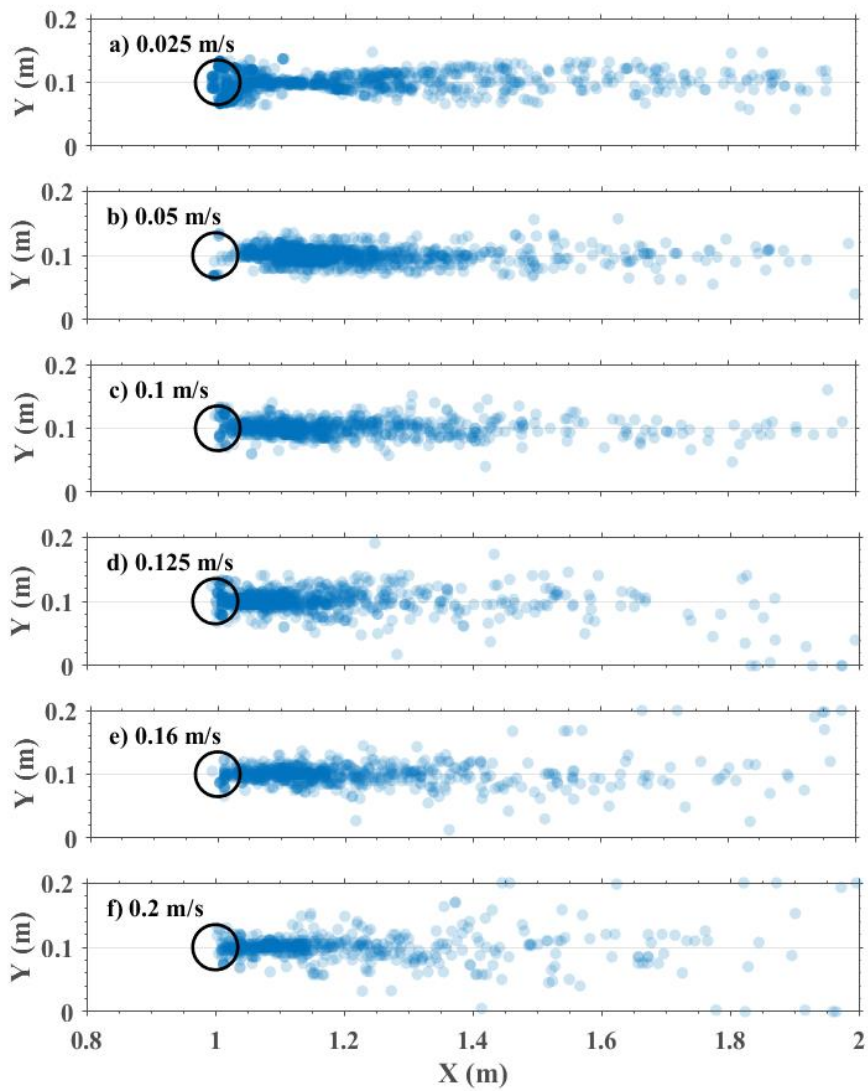
Figure 4.2 Fertilization position in xz plane
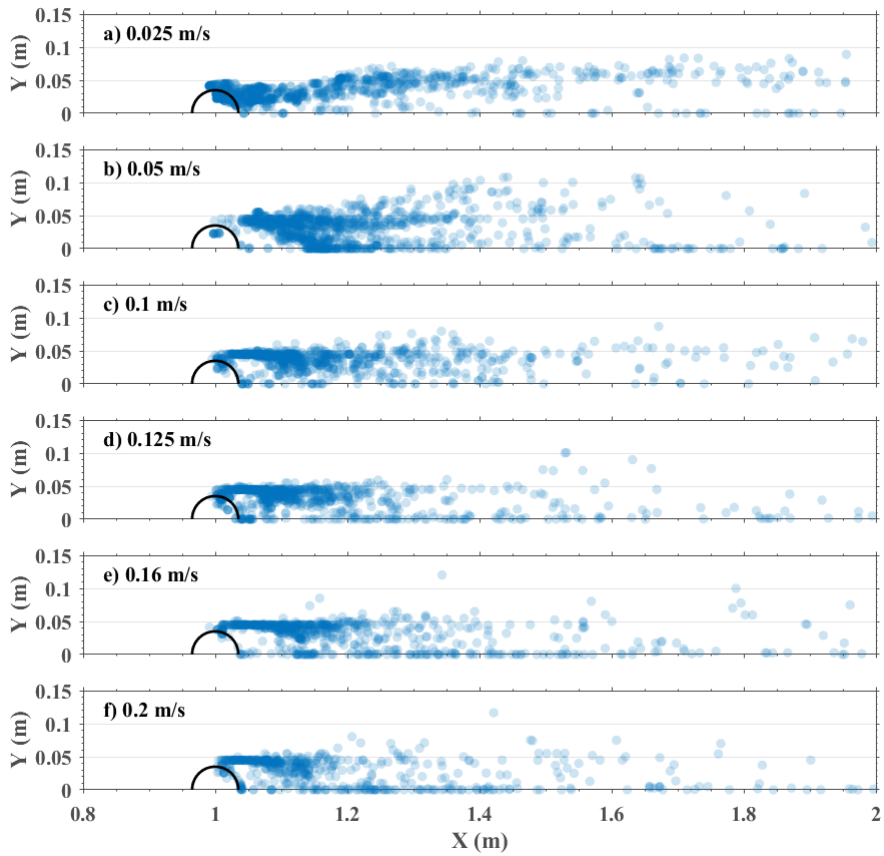
Figure 4.3 Fertilization position in xy plane

4.2 Flow structure analysis

When flow Reynolds number defined as $Re = \dfrac{UL}{\nu}$ is in the range between $180 < Re < 260$, wake structure of the circular cylinder changes from two dimensionality to three dimensionality (Williamson 1996). The flow Reynolds number for current study exist in the range between $2800 < Re < 16000$, when characteristic length is the diameter of the sea urchin body. It implies that flow structure behind the sea urchin body should be analyzed from three-dimensional perspective.

Figure 4.4 xz plane of instantaneous dimensionless flow structure contour for
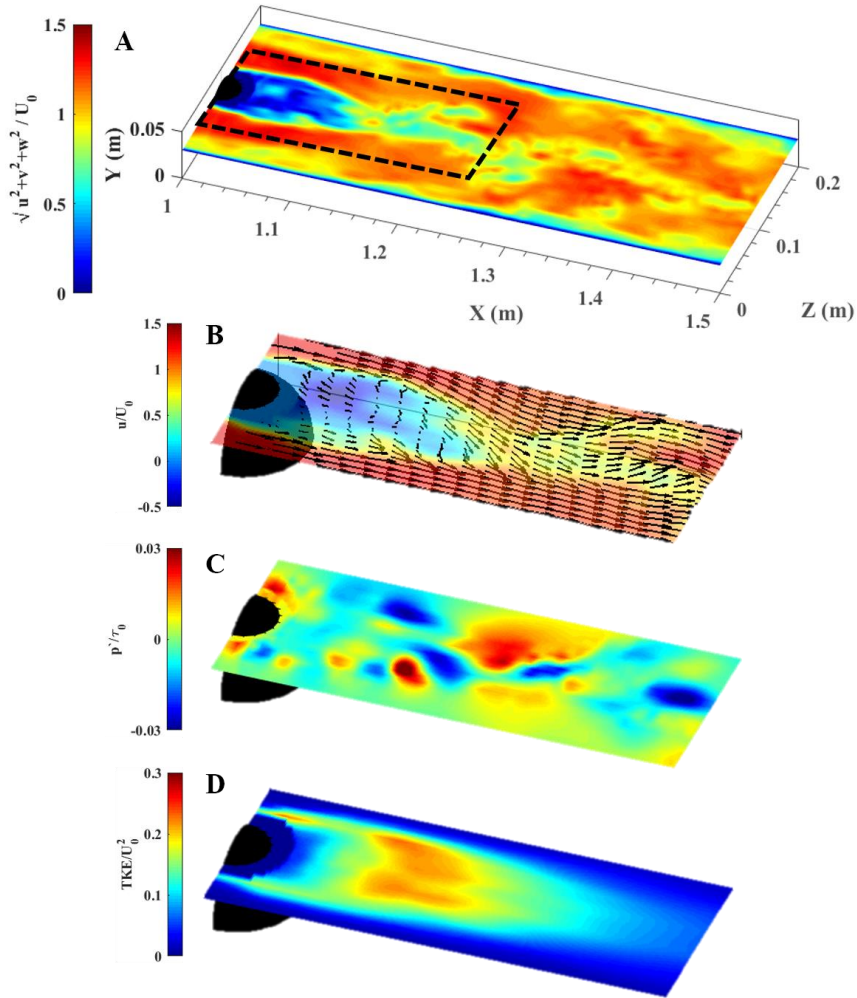y/H = 0.2. (A) Magnitude of velocity. Area marked with black dotted lines is
analyzed in more detail with various flow characteristics. (B) x directional velocity
with velocity vector for specified area in (A). (C) Pressure fluctuation for specified
area in (A). (D) Turbulent kinetic energy for specified area in (A).

Fig 4.4 depicts instantaneous flow structures in xz plane. Fig 4.4A shows that magnitude of velocity is the lowest at the right behind of the sea urchin body. The width of velocity fluctuation remains similar to the diameter of sea urchin body and the fluctuation dissipates far behind the sea urchin body. Area close to the female sea urchin body, where most fertilization process occurs and complex flow structures interact with gametes, is analyzed in detail. x-directional velocity vector plots suggest that backflow is generated and flow rotate inside the backflow region (Fig 4.4B). Pressure fluctuations which represent the vortex structures suggest that pockets of positive and negative pressure rotate after passing the recirculation region. Turbulent kinetic energy is largest at 0.1 m away from the sea urchin body. It corresponds to the region where pressure fluctuation is the largest and the position where recirculation zone terminates and x-directional velocity starts to recover its original velocity.
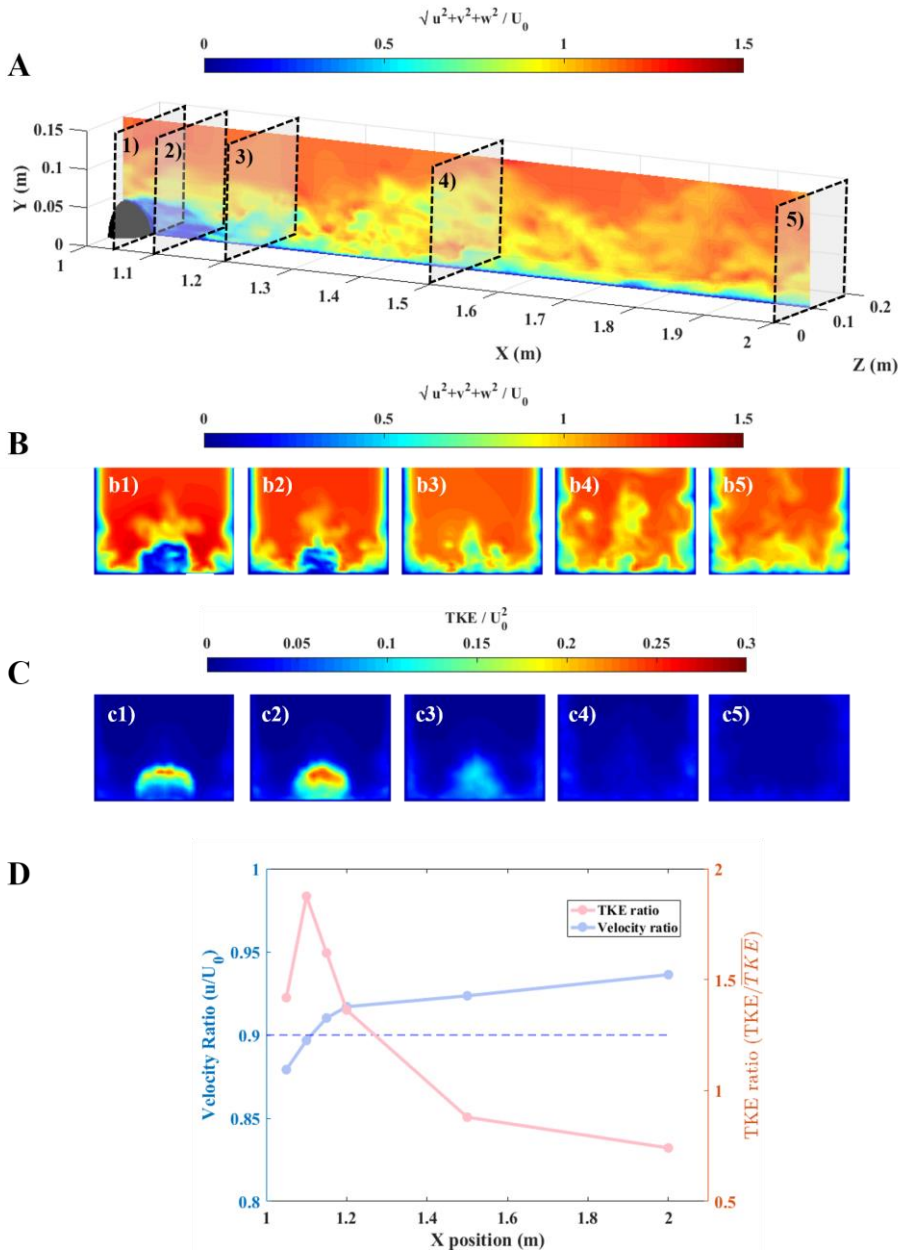
Figure 4.5 xy plane of instantaneous dimensionless flow structure contour for z/W
= 0.5. (A) Magnitude of velocity. yz plane of flow characteristics is depicted for the
location marked with black dotted line. 1) x = 1.05 (m), 2) x = 1.1 (m), 3) x = 1.2

(m), 4) x = 1.5 (m) 5) x = 2.0 (m) (B) Magnitude of velocity of yz plane for x position specified in (A). (C) Turbulent kinetic energy for x position specified in (A) (D) relative ratio of magnitude of velocity to inlet velocity and TKE to domain averaged TKE.

To determine the length that flow structures are influence by the sea urchin body at the downstream, the ratio of yz cross-sectional mean velocity to inlet velocity and cross-sectional mean turbulent kinetic energy is computed at each x positions. The ratio of flow characteristics are suggested in Tab 4.2

Table 4.2 Ratio of velocity magnitude to inlet velocity and TKE to domain averaged TKE

Distance from sea urchin (m)	0.05	0.1	0.15	0.2	0.5	1
$\overline{u_{yz}}/U_0$	0.879	0.897	0.910	0.917	0.924	0.936
$TKE/\overline{TKE}$	1.418	1.875	1.620	1.363	0.880	0.741

Fig 4.5A show that velocity magnitude is the lowest at the right behind of female sea urchin body and at the bottom. Velocity fluctuation intensifies in vertical direction as distance from the sea urchin body increases but in overall, velocity recovers its original inlet velocity as the distance from the center of the female sea urchin body gets further. When 0.1 m away, velocity reaches 90 % of its original velocity. Generation of turbulent kinetic energy is conspicuous until 1.2m, but at farther distance, the influence of sea urchin body on TKE is negligible. TKE is maximum at distance 0.1 m, and at 0.5 m distance, point TKE is lower than domain averaged value due to much of the dissipation of turbulence.

Based on the flow characteristics analyzed above, entire control volume behind the sea urchin body is divided into four subsections to further analyze the position where fertilization of sea urchin is most likely occur (Fig 4.6).

Aboral is defined as the region that the distance from the center of the female sea urchin body do not exceed 0.045 m. The radius of sea urchin is 0.04 m but to consider the eggs that are piled at the surface of sea urchin body, 0.045 m is selected as a boundary to define aboral area. For wake region, the distance from the center of sea urchin body do not exceed 0.1 m. TKE is maximum at this position and magnitude of velocity reaches 90 % of original inlet velocity. Substrate is the bottom region where transition of flow structure occurs. The distance should not exceed 0.3 m from the bottom, and 0.5 m from the center of the female sea urchin. Remaining areas are defined as water column where the influence of sea urchin body is negligible in this region and flow characteristics are similar to that of free stream flow.
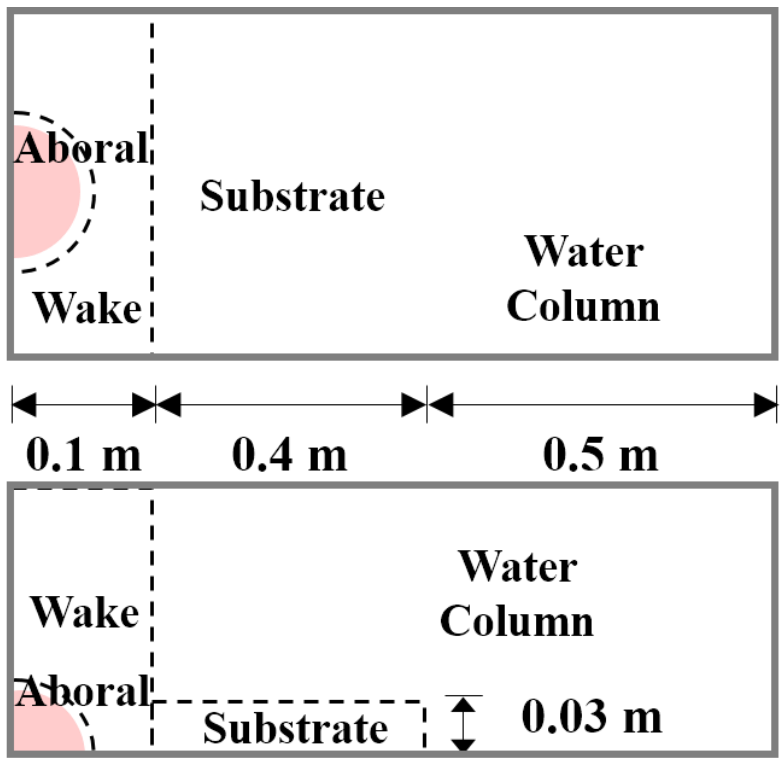
Figure 4.6 Divided sub-domains based on flow characteristic analysis.

4.3 Analysis of sea urchin fertilization process

4.3.1 Distribution of sea urchin gametes

The gametes of spawning animals are transported by the currents and turbulent diffusion in uni-directional flow (Kregting et al., 2013). Since transport of gametes rely on water motion, distribution of sperm and egg in the control volume vary by the flow velocity and elapse time of the simulation. In order to analyze collision and fertilization rates of gametes for different flow velocity, distribution of gametes depending on flow conditions are studied in beforehand.

Distance from the averaged position to individual position of gametes represents the magnitude of gamete distribution. If the values are large, particles are widely spread through the whole simulation domain and if small, gametes are concentrated to the center of the domain. Computed values of mean, variance and kurtosis of distances quantify the distribution of gametes which are suggested in Tab 4.3 and Tab 4.4.

Table 4.3 Statistical values of egg distribution

Velocity (m/s) Time(s)		0.025	0.05	0.1	0.125	0.16	0.2
5	μ_D	0.026	0.047	0.010	0.127	0.185	0.239
	$\sigma_D{}^2$	0.0001	0.0009	0.0041	0.0071	0.0148	0.0194
	κ	2.702	7.008	3.407	4.828	3.480	3.111
10	μ_D	0.041	0.096	0.208	0.253	0.257	0.245
	$\sigma_D{}^2$	0.0006	0.0036	0.0174	0.0197	0.0227	0.0198
	κ	1.838	7.051	2.713	2.371	1.760	1.893
20	μ_D	0.084	0.212	0.258	0.268	0.268	0.253
	$\sigma_D{}^2$	0.0040	0.0145	0.0189	0.0186	0.0188	0.0189
	κ	6.166	4.850	1.887	1.796	1.834	1.781

Table 4.4 Statistical values of sperm distribution

Velocity (m/s) Time(s)		0.025	0.05	0.1	0.125	0.16	0.2
5	μ_D	0.137	0.216	0.255	0.290	0.364	0.361
	$\sigma_D{}^2$	0.0069	0.0086	0.0237	0.0316	0.0412	0.0453
	κ	2.163	2.316	1.793	1.733	1.746	1.837
10	μ_D	0.157	0.242	0.368	0.375	0.378	0.352
	$\sigma_D{}^2$	0.0083	0.0142	0.0428	0.0435	0.0463	0.0447
	κ	2.393	2.180	1.960	1.900	1.824	1.821
20	μ_D	0.174	0.245	0.270	0.271	0.281	0.280
	$\sigma_D{}^2$	0.0125	0.0228	0.0268	0.0258	0.0265	0.0267
	κ	4.663	4.168	2.699	2.876	3.469	3.629

Mean and variance of both eggs and sperms increases as velocity increases and later converges after reaching velocity range 0.1 ~ 0.15 m/s. Kurtosis shows decreasing trend but later also converges at fast velocity. Such convergence of statistical values implies that the distributions of gametes are less affected by flow velocity after reaching velocity range 0.1 ~ 0.15 m/s. At low velocity, transport of gametes relies on currents rather than being mixed by wake and turbulent diffusion. It leads gametes to move in clumped pattern rather than being randomly distributed in the entire domain. Distance between sperms show higher mean and variance and lower kurtosis compared to distance between eggs. It suggests that sperms are more likely to be distributed than eggs at the time of collision or fertilization.
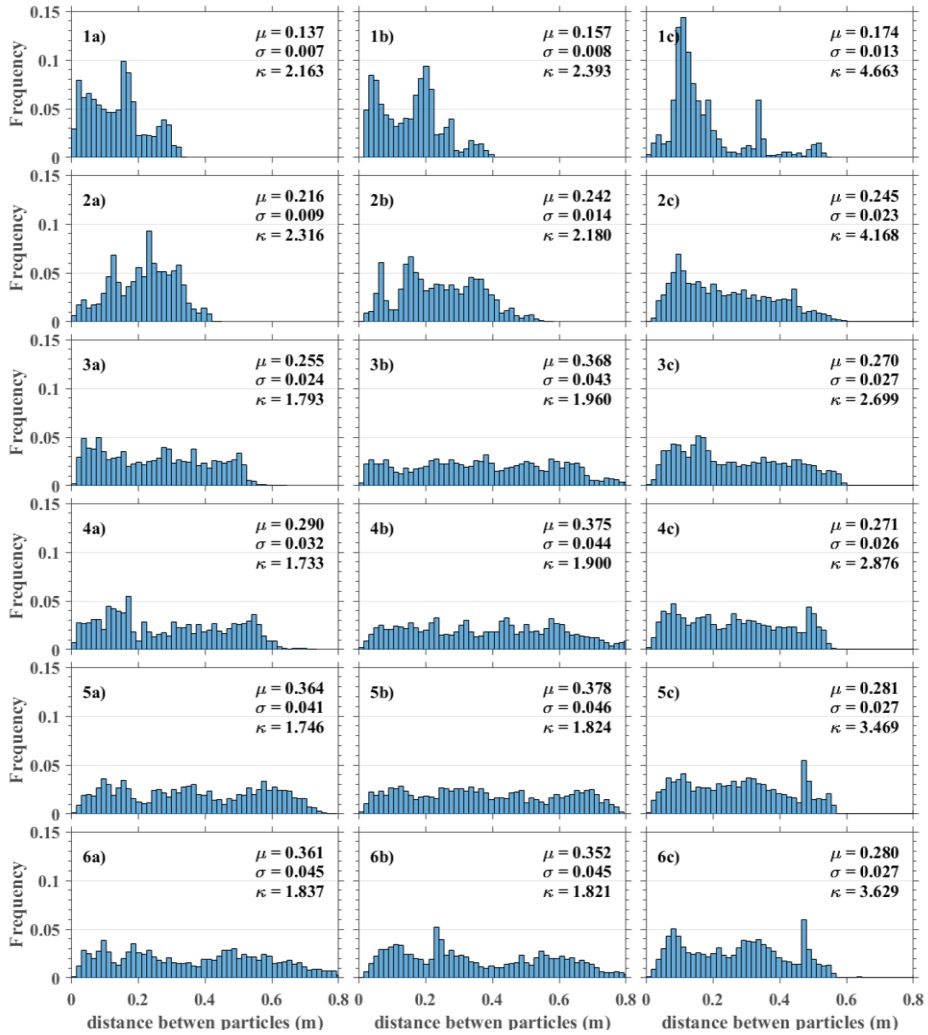
Figure 4.7 Distance between sperms in the control volume. (A) Elapse time, t = 5 (s). (B) Elapse time, t = 10 (s). (C) Elapse time, t = 20 (s). The numbers in the picture sub titles, 1 -6 respectively refer to simulation result for varying inlet velocity, v = 0.025, 0.05, 0.1, 0.125, 0.16, 0.2 m/s.

Fig 4.7 suggest the histogram of distances between sperms and averaged position of sperms. At the initial stages of the gamete injection, distance between sperms increases by dispersion and sperms become better distributed as velocity increases. Results of low velocity shows heterogeneous distribution of gametes with high kurtosis while homogenous distribution of gametes are observed for high velocity case with low kurtosis. Histogram of eggs also show similar trends with Fig 4.7

Morista index is another measure to quantify the heterogeneity of gametes. Fig 4.8 shows Morista index for eggs and sperms at each time step which shows decreasing index of both gametes as the elapse time and flow velocity increases. Gametes are injected from head of sea urchin as a cluster and become gradually distributed inside the simulation domain as time passes due to surrounding flow, leading to decreasing index.

The variation of the index is large at low velocities which implies that velocity is influential to alter gamete distributions at low velocities. As velocity reaches certain values, increasing velocity do not cause additional changes to gamete distribution and thus Morista index of both gametes also converges. Subplots in Fig.15 shows time-averaged Morista index corresponding to flow velocity and it shows that I_p remains similar after 0.1 m/s. Values of time averaged Morista index are suggested in 4.5.
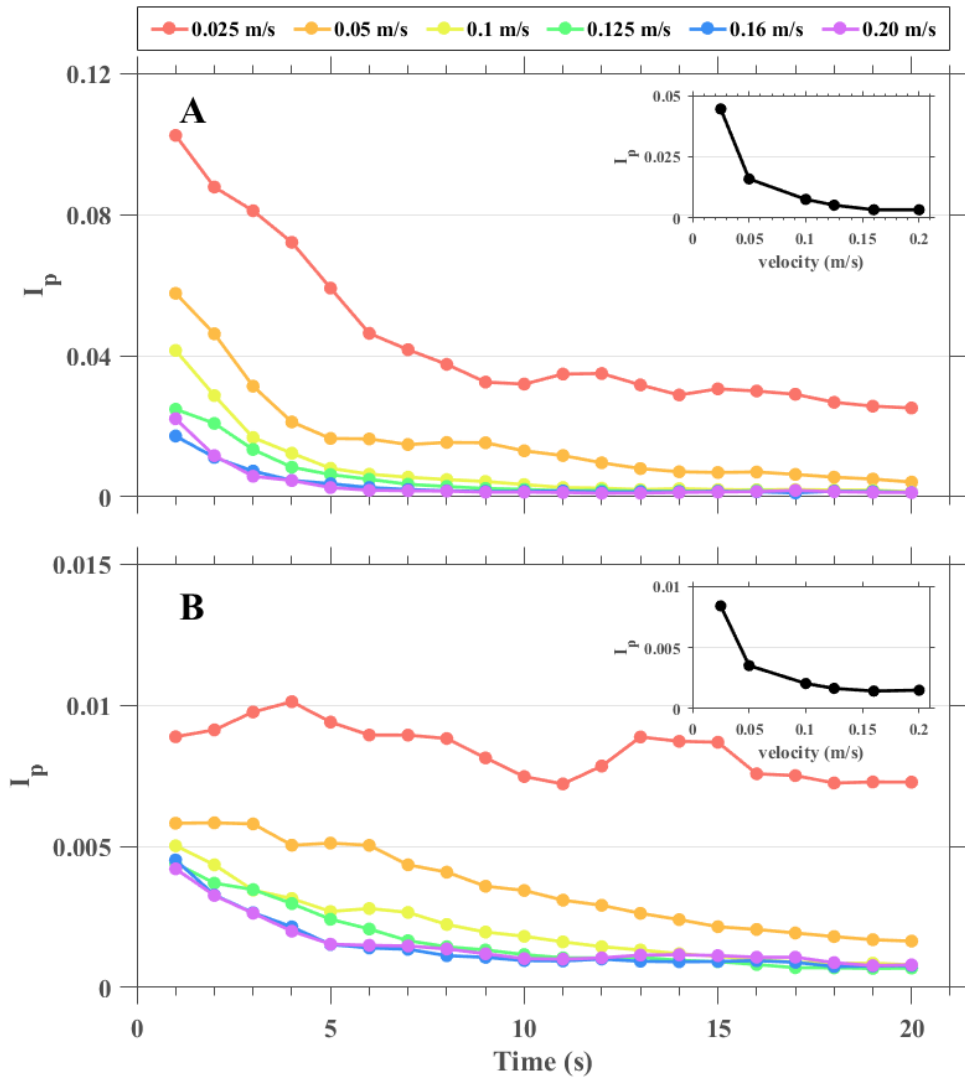
Figure 4.8 Morista index of gametes at each time step starting from the injection time of eggs. (A) Index of eggs (B) Index of sperms. Subplots in each figure show timea-averaged Morista index for varying flow velocit

Table 4.5 Time averaged Morista index for sperms and eggs

	0.025	0.05	0.1	0.125	0.16	0.2
Eggs	0.0445	0.0160	0.0077	0.0053	0.0034	0.0034
Sperms	0.0084	0.0035	0.0021	0.0017	0.0014	0.0015

In order to analyze gamete distribution based on flow structures, integral time scales which measures the length of time that particles of certain position would be influenced by previous time step is calculated. Fig 4.9A represents the histogram of integral time scale at each grid point. At low velocity, wide range of integral time scale exists in the domain, which implies that dimensions of flow structures are heterogeneous. Heterogeneous distribution of gametes at low velocity (Fig 4.8) could be explained by similar trend in flow structures.

Averaged integral time scale reaches 33.5 second showing that memory lasts long for particle trajectories and particle positions are correlated through long simulation time which lead to long integral time scale. As velocity increases, both mean and variance of integral time scale decreases and at 0.2 m/s of inlet velocity, average integral time scale reaches 3.5 seconds. At fast velocity flow structures become homogenous and integral time scale corresponding to each grid point have similar values, identical to homogenous gamete distribution in high velocities.

Assuming Taylor's Frozen-in hypothesis, integral length scale can be computed by multiplying representative integral time scale of simulation domain to inlet velocity and the results are represented in Fig 4.9B.
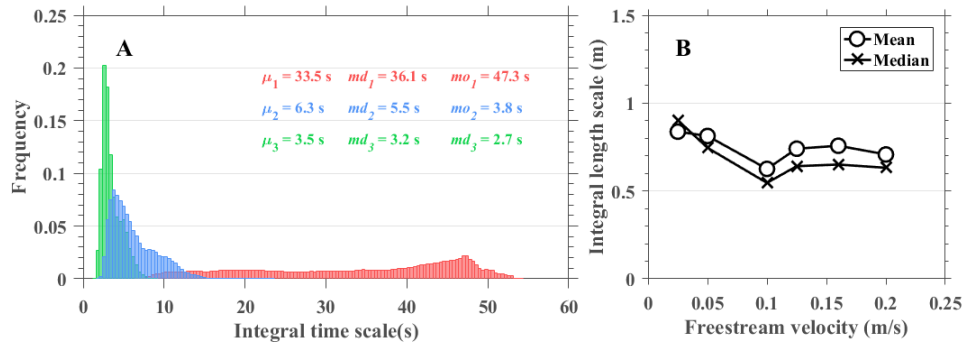
Figure 4.9 (A) Histogram of integral time scale computed at every grid point of entire domain for different inlet velocity. █ : 0.025 m/s; █ : 0.1 m/s; █ : 0.2 m/s. (B) Integral length scale computed based on Frozen-in hypothesis with mean and median integral time scale.

Integral length scale is the representative length scale of flow structures or the largest eddy size in the domain. For low velocity, integral length scale is high which implies that eddy size is comparatively large. Clusters of gametes are less likely to be broken when eddy size is large and gametes are less distributed in the simulation domain. At low velocities, gametes are transported by background currents before being distributed by wake structures to maintain clusters from initial injection time. It leads to high Morista index implying heterogeneous distribution of gametes.

At 0.1 m/s of free-stream velocity, integral length scale reaches minimum and remains to similar values even at faster velocities. When eddy size decreases, it generates effective disturbance to break clusters of gametes and distribute them into wider area. Thus, low Morista index is computed, which represents homogenous distribution of gametes. Negligible variation of integral length scale after 0.01 m/s implies that eddy size and dimension of wake structures do not vary by increasing flow velocity and the effect of flow on gamete distribution has converged. It explains why Morista index converges at 0.1 m/s.

4.3.2 Sperm density

Sperm concentration is a dominant factor to determine the success of fertilization and should exceed $10^6 / l$ to maintain fertility of sperms. When sperm concentration satisfies the condition, fertilization occurs if sperm and egg collide with each other. Spatial averaged sperm concentration for each time step is suggested for varying inlet velocity in Fig 4.10.
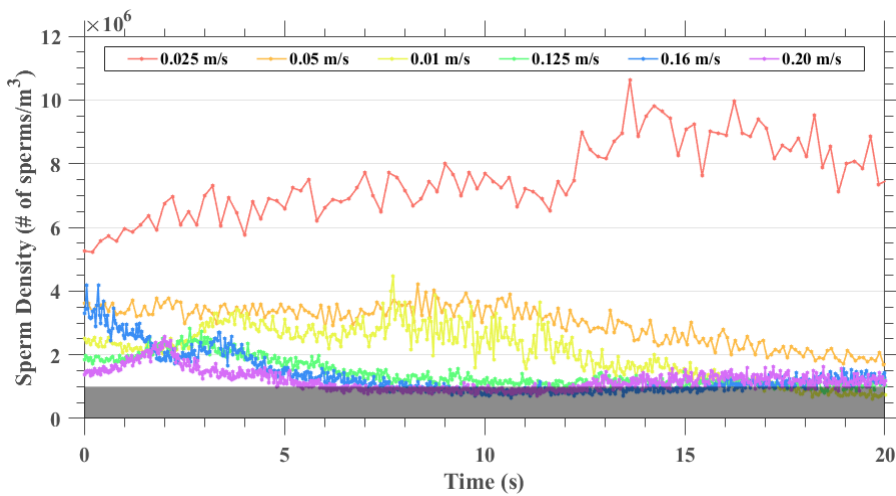
Figure 4.10 Spatial averaged sperm concentration at each time step starting from the injection time of eggs. Grey area represents the condition when sperms loose fertility due to low concentration.

It shows that at fast velocities, spatial averaged sperm concentration is lower than $10^6 / l$ during most of the elapse time. Comparatively the influence of sperm density on fertilization would be dominant as flow velocity increases.

Decreasing trend of sperm concentration can be explained by the variation of turbulent mixing as flow velocity increases. Below Fig 4.11 shows turbulence values for varying flow velocity. The order of dissipation and shear production is identical for most locations. As velocity increases, both shear production and dissipation increases (Fig 4.11A), but relative amount of production compared to dissipation prevails (Fig 4.11B). The ratio between shear production and dissipation increases as flow velocity increases. As a result, turbulence energy in the domain increases as flow velocity increases leading to higher turbulent mixing.
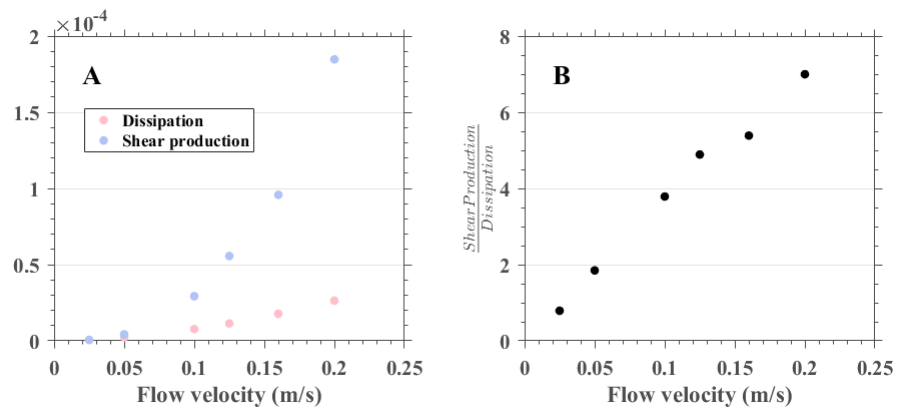
Figure 4.11 Domain-averaged turbulence characteristics; (A) dissipation and shear

production, (B) Ratio between produced to dissipated turbulence energy.

4.3.3 Analysis of contact rate and fertilization rate

Increasing collision rate until 0.125 m/s (Fig 4.1) can be explained by decreasing integral length scale (Fig 4.9). As gametes are injected from head of the sea urchin, they cluster based on surrounding flow structures which is the eddy. It is likely that eggs and sperms located in an identical eddy would collide and fertilize. For effective collision between gametes, the eddy size should be small enough to cause overlap between the locations of egg clusters and sperm clusters. Decreasing trend of Morista index until 0.1 m/s also corresponds to increasing collision rate until 0.125 m/s. It shows that at low velocity, Morista index is high and gametes are insufficiently mixed enough to bring effective collision.

When increasing flow velocity has negligible effect on eddy size and the magnitude of gamete clusters after 0.1 m/s, sperm concentration has a dominant effect on the gamete collision. If excessive mixing is caused, gametes are distributed into wider domain, reducing the possibility of collision between eggs and sperms.

Fertilization rate is directly influenced by sperm concentration since sperm fertility depends on the sperm concentration. When flow velocity reaches 0.125 m/s, sperm concentration becomes lower than $10^6 / l$ at certain time step, and the duration of low sperm concentration increases as velocity increases. It leads to deceasing fertilization rate for increasing velocity.

Collision between gametes which rely on wake structures should be preceded for fertilization to occur. However, sperm concentration, which rely on turbulent mixing acts as a dominant factor to determine the fertilization rate.

4.4 Relative contribution of different locations on fertilization

Control volume behind the sea urchin body is divided into four subsections based on the flow characteristics (Fig 4.6) and the relative contribution of each location on collision and fertilization varies by flow velocities (Fig 4.12).

At the lowest velocity, aboral surface have dominant contribution on both collision rate and fertilization rate. As velocity increases the contribution of aboral surface rapidly decreases, and in contrast, the contribution of wake and substrate increases. Regardless of flow velocity, water column has least contribution to the fertilization among locations. Previous research shows that fertilization occurs most frequently close to the female sea urchin body under any flow velocities (Thomas et al. 2013). The difference between the result of precedent and corresponding study can be explained by inevitable different conditions between laboratory experiment and numerical simulation.
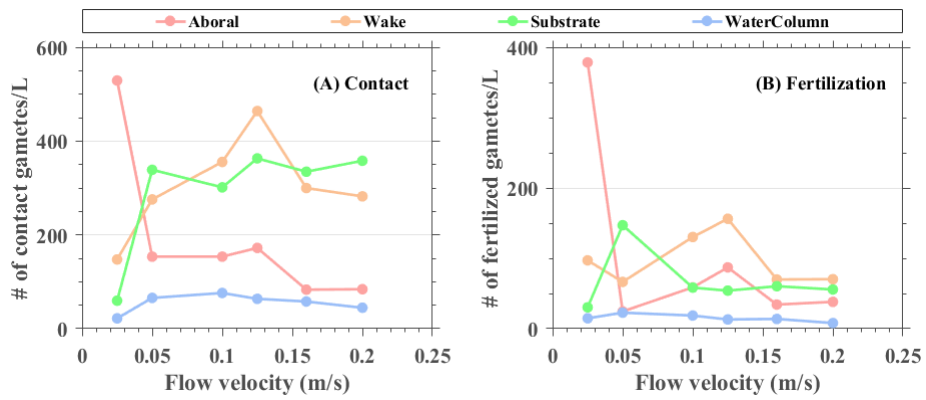
Figure 4.12 Number of contact and fertilized gametes per unit volume in each sub-

domain. (A) Contact rate (B) Fertilization rate

First, due to difficulties to count fertilized eggs, wake region was excluded from analysis in laboratory experiment. If wake region is assumed as being close to female sea urchin body and the number of fertilized eggs for aboral and wake are added together, results of numerical simulation corresponds to that of laboratory experiment and the relative contribution of aboral surface becomes dominant.

Limitations of numerical simulation leads to decreased contribution of aboral surface. Adhesion between gametes cause them to be piled up at the aboral regions, enhancing the possibility of fertilization, but adhesion force was neglected for corresponding study. Simplification of sea urchin body as hemisphere without spines also influences to underestimate the relative contribution of aboral area on fertilization. Spines trap gametes inside and elongate the residence time. The absence of spines causes subtle changes to the influence of sea urchin body on gamete distribution and relative contribution of each locations.

Turbulence values are computed for each location to analyze their variation due to increasing velocity and the results are suggested in Fig 4.13.
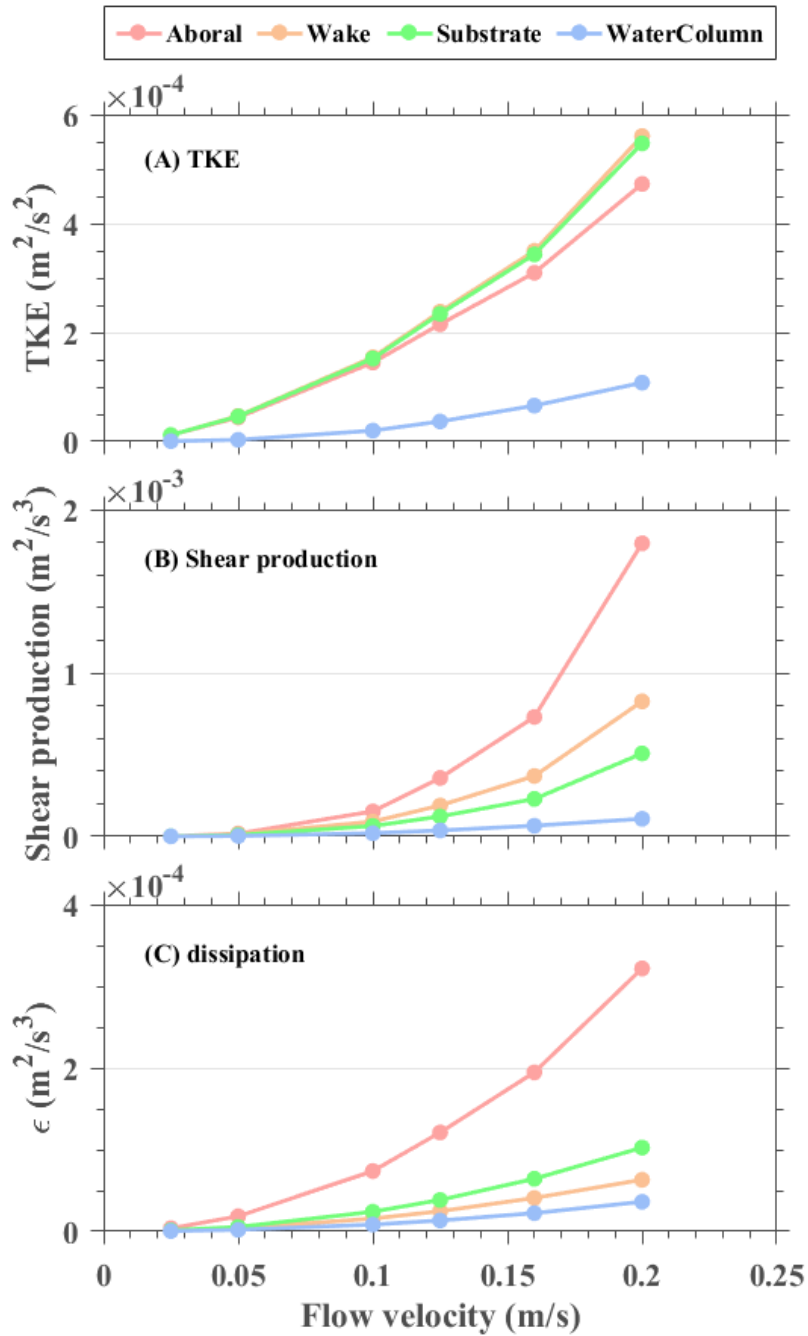
Figure 4.13 Flow characteristics in each sub-domain. (A) Turbulent kinetic energy

(B) Shear production (C) Dissipation

Turbulence kinetic energy is the largest at wake and substrate followed by aboral and water column (Fig 4.13A). This order is similar to the order of relative contribution of location on fertilization. Compared to other locations, turbulence properties (turbulence kinetic energy, shear production and dissipation) are low at the water column, and the values are close to open-channel flow characteristics when sea urchin body is not located inside the simulation domain. In other words, sea urchin body act as a driving force to stimulate fertilization and collision process by changing hydrodynamic structures and flow characteristics.

CHAPTER 5. CONCLUSION

5.1 Summary

The objective of present study is to analyze the flow effects on sea urchin fertilization. CFD simulation was carried out by introducing Lagrangian Particle Tracking algorithm as an effective tool to compute trajectories of colliding and fertilizing gametes while obtaining background flow fields at the same time. Laboratory experiment having same conditions with numerical simulation validated that CFD reasonably represents flow structures in real condition.

Fertilization occurs when two conditions are satisfied between egg and sperm; 1) the distance between the center of eggs and sperms should be less than the sum of egg radius, sperm radius and egg jelly coat thickness, which is the definition of collision in present study; 2) sperm concentration should exceed $10^6 / l$ to maintain fertility and activate the chemical interaction between sperm and egg for fertilization. Collision and fertilization rate was estimated for 6 flow velocity cases ranging from 0.025 – 0.2 m/s at uni-directional flows.

As velocity increases, collision rate increased until 0.125 m/s and started to decrease at higher velocities. On the other hand, fertilization steadily decreased by increasing flow velocity. To interpret the influence of flow on collision and fertilization, particle distributions were first analyzed. Distance between instantaneous location and mean position of gametes were calculated which showed

that the gametes are more distributed as elapse time and background flow velocity increases. Another method to quantify gamete distribution is to compute Morista index which represents the heterogeneity of gamete distribution. Until 0.1 m/s, the heterogeneity of gamete distribution evidently decreased and started to converge at faster velocities. It is expected that mean flow velocities have dominant influence on gametes distribution until 0.1 m/s and the effect diminishes for faster flow velocities.

Integral time scale and integral length scale was computed to analyze the relationship between flow characteristics and gamete distribution. Integral length scale which represents the largest eddy size reached minimum at 0.01 m/s when flow velocity was increased, but showed negligible variation at faster velocities. Similar trend between heterogeneity of gamete distribution and integral length scale shows that eddy size influence how well gamete would be distributed, and further how effectively gametes could collide with each other.

Sperm concentration steadily decreased as flow velocity increased and the time duration of sperm loosing fertility due to low concentration increased. It corresponds to steadily decreasing fertilization rate at increasing velocity. The rate of shear production to dissipation increased as velocity increased leading to high turbulent mixing. Turbulence act as a force to mix gametes and lower sperm concentration.

The relative contribution of different locations was highest in aboral surface for lowest velocity 0.25 m/s. For higher velocities, wake and substrate showed significance over other regions. Analysis of turbulence characteristics showed that the region having highest turbulence kinetic energy has most contribution to total

fertilization.

5.2. Recommendation and future works

Present study suggested CFD as a possible method to analyze external fertilization process. The actual flow conditions of sea urchin habitat are diverse including oscillatory flows, rotating flow and stationary flows. Precedent studies that relied on laboratory experiment considered various flow conditions but includes inevitable limitations and detailed analysis becomes unavailable. Due to easy accessibility and wide applicability, CFD suggest possibility of detailed analysis about fertilization occurring in various flow conditions and future studies focusing on varied flow conditions based on CFD would suggest thorough understanding about the fertilization process of sea urchin.

Although validation of CFD was proceeded with flow velocity for present study, comparison between particle trajectories of numerical simulation and laboratory experiments should be also considered to test the validity of Lagrangian Particle Tracking algorithm. Numerous previous studies about validation for single particle trajectories exist but validation for particles moving in clusters lack and such studies are expected as future works.

Neglected characteristics of sea urchin should be also considered for future studies. Complex geometry of sea urchin surface was assumed as simple hemisphere and the cohesion between gametes were also disregarded for present studies. If the effect of sea urchin characteristics on fertilization rate could be considered by numerical simulation reasonably, real fertilization mechanism could be analyzed in detail.

REFERENCES

Argyropoulos, C. D., & Markatos, N. C. (2015). Recent advances on the numerical modelling of turbulent flows. *Applied Mathematical Modelling*, *39*(2), 693-732.

Crank, J. (1975). The mathematics of difiusion. *2nd end*.

Crimaldi, J. P., & Browning, H. S. (2004). A proposed mechanism for turbulent enhancement of broadcast spawning efficiency. *Journal of Marine Systems*, *49*(1-4), 3-18.

Crimaldi, J. P. (2012). The role of structured stirring and mixing on gamete dispersal and aggregation in broadcast spawning. *Journal of Experimental Biology*, *215*(6), 1031-1039.

Crimaldi, J. P., & Zimmer, R. K. (2014). The physics of broadcast spawning in benthic invertebrates. *Annual Review of Marine Science*, *6*, 141-165.

Denny, M. W., & Shibata, M. F. (1989). Consequences of surf-zone turbulence for settlement and external fertilization. *The American Naturalist*, *134*(6), 859-889.

Denny, M. W., Nelson, E. K., & Mead, K. S. (2002). Revised estimates of the effects of turbulence on fertilization in the purple sea urchin, Strongylocentrotus purpuratus. *The Biological Bulletin*, *203*(3), 275-277.

Denny, M. (2014). *Biology and the mechanics of the wave-swept environment*. Princeton University Press.

Elghobashi, S. (1994). On predicting particle-laden turbulent flows. *Applied scientific*

research, *52*(4), 309-329.

Farley, G. S., & Levitan, D. R. (2001). The role of jelly coats in sperm-egg encounters, fertilization success, and selection on egg size in broadcast spawners. *The American Naturalist*, *157*(6), 626-636.

Fish, F. E., & Lauder, G. V. (2006). Passive and active flow control by swimming fishes and mammals. *Annu. Rev. Fluid Mech.*, *38*, 193-224.

Fraga, B., Stoesser, T., Lai, C. C., & Socolofsky, S. A. (2016). A LES-based Eulerian–Lagrangian approach to predict the dynamics of bubble plumes. *Ocean modelling*, *97*, 27-36.

Greifzu, F., Kratzsch, C., Forgber, T., Lindner, F., & Schwarze, R. (2016). Assessment of particle-tracking models for dispersed particle-laden flows implemented in OpenFOAM and ANSYS FLUENT. *Engineering Applications of Computational Fluid Mechanics*, *10*(1), 30-43.

Hill, R. J. (1996). Corrections to Taylor's frozen turbulence approximation. *Atmospheric Research*, *40*(2-4), 153-175.

Inamdar, M. V., Kim, T., Chung, Y. K., Was, A. M., Xiang, X., Wang, C. W., ... & Sastry, A. M. (2007). Assessment of sperm chemokinesis with exposure to jelly coats of sea urchin eggs and resact: a microfluidic experiment and numerical study. *Journal of Experimental Biology*, *210*(21), 3805-3820.

James P. and Siikavuopio S. (2011) A guide to the sea urchin reproductive cycle and staging sea urchin gonad samples. Nofima. ISBN: 978-82-7251-976-5.

Ji, B., Luo, X. W., Peng, X. X., & Wu, Y. L. (2013). Three-dimensional large eddy

simulation and vorticity analysis of unsteady cavitating flow around a twisted hydrofoil. *Journal of Hydrodynamics*, *25*(4), 510-519.

Kregting, L. T., Bass, A. L., Guadayol, Ò., Yund, P. O., & Thomas, F. I. (2013). Effects of oscillatory flow on fertilization in the green sea urchin Strongylocentrotus droebachiensis. *PloS one*, *8*(9), e76082.

Kregting, L. T., Thomas, F. I., Bass, A. L., & Yund, P. O. (2014). Relative effects of gamete compatibility and hydrodynamics on fertilization in the green sea urchin Strongylocentrotus droebachiensis. *The Biological Bulletin*, *227*(1), 33-39.

Kundu, P. K., & Cohen, I. M. (2008). Fluid mechanics. 2004. *Elsevier Acad. Press, London*, *199*, 400.

Lawrence, J. M. (Ed.). (2013). *Sea urchins: biology and ecology*(Vol. 38). Academic Press.

Levitan, D. R., Sewell, M. A., & Chia, F. S. (1992). How distribution and abundance influence fertilization success in the sea urchin Strongylocentotus franciscanus. *Ecology*, *73*(1), 248-254.

Levitan, D. R. (1993). The importance of sperm limitation to the evolution of egg size in marine invertebrates. *The American Naturalist*, *141*(4), 517-536.

Liu, H., Wassersug, R. I. C. H. A. R. D., & Kawachi, K. E. I. J. I. (1997). The three-dimensional hydrodynamics of tadpole locomotion. *Journal of Experimental Biology*, *200*(22), 2807-2819.

Mead, K. S., & Denny, M. W. (1995). The effects of hydrodynamic shear stress on fertilization and early development of the purple sea urchin Strongylocentrotus

purpuratus. *The Biological Bulletin*, *188*(1), 46-56.

Nicoud, F., & Ducros, F. (1999). Subgrid-scale stress modelling based on the square of the velocity gradient tensor. *Flow, turbulence and Combustion*, *62*(3), 183-200.

Nortek, A. S. (2009). Vectrino velocimeter user guide. *Nortek AS, Vangkroken, Norway*, *621*.

Pavlov, V. V., & Rashad, A. M. (2012). A non-invasive dolphin telemetry tag: computer design and numerical flow simulation. *Marine Mammal Science*, *28*(1).

Pennington, J. T. (1985). The ecology of fertilization of echinoid eggs: the consequences of sperm dilution, adult aggregation, and synchronous spawning. *The Biological Bulletin*, *169*(2), 417-430.

Longest, P. W., & Vinchurkar, S. (2007). Effects of mesh style and grid convergence on particle deposition in bifurcating airway models with comparisons to experimental data. *Medical engineering & physics*, *29*(3), 350-366.

Roache, P. J. (1994). Perspective: a method for uniform reporting of grid refinement studies. *Journal of Fluids Engineering*, *116*(3), 405-413.

Rocha, P. C., Rocha, H. B., Carneiro, F. M., da Silva, M. V., & de Andrade, C. F. (2016). A case study on the calibration of the k–ω SST (shear stress transport) turbulence model for small scale wind turbines designed with cambered and symmetrical airfoils. *Energy*, *97*, 144-150.

Savory, E., & Toy, N. (1986). The flow regime in the turbulent near wake of a hemisphere. *Experiments in Fluids*, *4*(4), 181-188.

Smith-Gill, S. J. (1975). Cytophysiological basis of disruptive pigmentary patterns in

the leopard frog Rana pipiens. II. Wild type and mutant cell-specific patterns. *Journal of Morphology*, *146*(1), 35-54.

Taylor, G. I. (1938). The spectrum of turbulence. *Proceedings of the Royal Society of London. Series A-Mathematical and Physical Sciences*, *164*(919), 476-490.

Thomas, F. I., Kregting, L. T., Badgley, B. D., Donahue, M. J., & Yund, P. O. (2013). Fertilization in a sea urchin is not only a water column process: effects of water flow on fertilization near a spawing female. *Marine Ecology Progress Series*, *494*, 231-240.

Tomboulides, A. G., & Orszag, S. A. (2000). Numerical investigation of transitional and weak turbulent flow past a sphere. *Journal of Fluid Mechanics*, *416*, 45-73.

Uijttewaal, W. S. J., & Oliemans, R. V. A. (1996). Particle dispersion and deposition in direct numerical and large eddy simulations of vertical pipe flows. *Physics of Fluids*, *8*(10), 2590-2604.

Vogel, H., Czihak, G., Chang, P., & Wolf, W. (1982). Fertilization kinetics of sea urchin eggs. *Mathematical Biosciences*, *58*(2), 189-216.

Williamson, C. H. (1996). Vortex dynamics in the cylinder wake. *Annual review of fluid mechanics*, *28*(1), 477-539.

White, F. M. (2003). Fluid mechanics. 5th. *Boston: McGraw-Hill Book Company*.

Zhang, Z., & Chen, Q. (2007). Comparison of the Eulerian and Lagrangian methods for predicting particle transport in enclosed spaces. *Atmospheric environment*, *41*(25), 5236-5248.

국문초록

흐름이 성게 수정에 미치는 영향

서울대학교 대학원

건설환경공학부

유 호 정

해저 경계층 내부의 복잡한 유체역학적 구조는 해양 생태계의 다양한 생물학적 현상을 지배하는 주요 인자이다. 성게의 번식 과정은 체외수정을 통해 이루어지며 경계층 내의 흐름 조건에 의존한다. 따라서 성게의 수정 과정을 역학적으로 설명하기 위해서는 주변 유체에 대한 이해가 선행되어야 한다. 일반적으로 거친 바닥과 유선형 물체 뒤에서는 난류 경계층이 형성되며, 경계층 내부의 급격한 유체 구조 변화는 난류 혼합을 발생시킨다. 성게의 몸체에서 방류된 생식 세포는 이러한 난류 혼합에 의해 서로 만나고 수정된다.

본 연구의 목적은 성게 수정에 위치가 미치는 영향을 흐름 조건에 따라 파악하는 것이다. 단일 방향 흐름 조건에서 유속 범위가 0.025 – 0.05

m/s 일 때, 수정률을 계산하였으며 소 영역별로 (Aboral, Wake, Substrate, Water Column) 전체 수정률에 미치는 상대적 영향력을 파악하였다. 속도가 증가할수록, 수정률은 감소하는 형상을 보였으며, 전반적으로 Wake지역에서 가장 많은 수정이 일어났다. 연구는 3단계로 진행되며 순서는 다음과 같다. 첫 번째, 수치 모의를 통해 구조물 후류의 구조를 파악하고 입자 확산 궤적을 Lagrangian Particle Tracking (LPT)을 통해 구현한다. 두 번째, 난자와 정자 사이의 거리와 정자의 밀도를 바탕으로 수정된 생식세포를 파악한다. 마지막 단계는 유체 구조를 바탕으로 총 4개로 나뉜 소 영역이 전체 수정에 미치는 상대적 영향력을 분석한다.

본 연구는 선행연구에서 실험으로 모의한 성게의 수정 과정을 수치 모델링을 통해 구현하고 역학적 관점으로 확장하여 분석하는데 의의가 있다. 본 연구에 적용된 방법론을 통해 난류 확산과 입자 사이의 반응 작용에 의해 발생하는 다양한 공학적 자연과학적 현상을 연구 할 수 있으며 입자의 궤적과 유속 장을 동시에 계산해야하는 복잡한 문제에 대한 해결책을 제시한다.